



**Abstract**

The presence of a pore fluid is recognized to significantly increase the mobility of saturated over dry granular flows. However, experimental studies in which both the bulk-scale (runout) and grain-scale behaviour of identical granular material in a dry and saturated initial state are directly compared are rare. Further, the mechanisms through which pore fluid increases mobility may not be captured in experimental flows of small volume typical of laboratory conditions. Here we present the results of dry and initially fluid saturated or “wet” experimental flows in a large laboratory flume for five source volumes of 0.2 to 1.0 m<sup>3</sup>. Our results demonstrate that the striking differences in the nature of interactions at the particle scale between wet and dry flows can be directly linked to macro-scale behaviour: in particular, a greatly increased mobility for wet granular flows compared to dry, and a significant influence of scale as controlled by source volume. This dataset provides valuable test scenarios to explore the fundamental mechanisms through which the presence of a pore fluid increases flow mobility by first constraining the frictional properties of the material (dry experiments), permitting an independent evaluation of the implementation of interstitial fluid effects in numerical runout models (wet experiments).

**Plain Language Summary**

An accurate prediction of how fast and how far a landslide, such as a debris flow, will travel is essential to define the hazard posed to life and property by these geophysical flows. While dry frictional flows often behave according to the simple physics of friction resisting motion, water saturated granular flows tend to travel farther and faster than the same scenario under dry conditions. In this paper we explore this phenomenon in detail, using high-speed image analysis to look for and quantify differences in grain-scale behaviour that might lead to increased mobility in saturated over dry flows, and high definition laser scans to quantify how far the debris travelled. Large flume tests comparing dry versus saturated flows for five source volumes of 0.2 to 1.0 cubic metres reveal that, in contrast to dry flows, saturated flows travel significantly farther as the volume of the landslide increases. This data is unique as it will enable researchers to test how well numerical simulations are able to model the travel behaviour of the same material in a dry and water saturated state.

**1 Introduction**

The quantification of the hazard posed by a potential landslide source volume requires an accurate prediction of the travel path and distal reach of the debris. This is generally accomplished in practice by using runout observations from past landslide events in the same location or similar geologic materials to delineate potential hazard areas for future landslides. These observations are then used either within an empirical-statistical approach to define runout exceedance probability (Legros, 2002) or by inferring debris rheological models and parameters from numerical simulations to match runout and inundation depth trimlines of historical events (McDougall, 2017). Heim’s Ratio ( $H/L$ ) was an early empirical-statistical proposal of a parameter for risk assessment by geometrical similarity (Figure 1). The total runout length  $L$  has the components of translation of the centre of mass  $L_{COM}$  and spreading of the material ahead of the centre-of-mass  $S_f$  (Dade & Huppert, 1998; Staron & Lajeunesse, 2009), while the difference in elevation,  $H$ , is measured from the back of the head scarp to the front of the debris. The total runout length  $L$  is typically of greatest interest for hazard assessment whereas the potential energy of the source volume is often equated to  $H$ . As a further development to Heim’s Ratio, Parez & Aharonov (2015) then presented a functional model in which the contribution of spreading of the material is related to channel geometry as well as the surface angle of the final deposit.

The travel angle  $\alpha_g$  is defined as the angle of declination between the centre of mass of the source volume and the centre of mass of the runout deposit ( $H_{COM}/L_{COM}$ ) and has

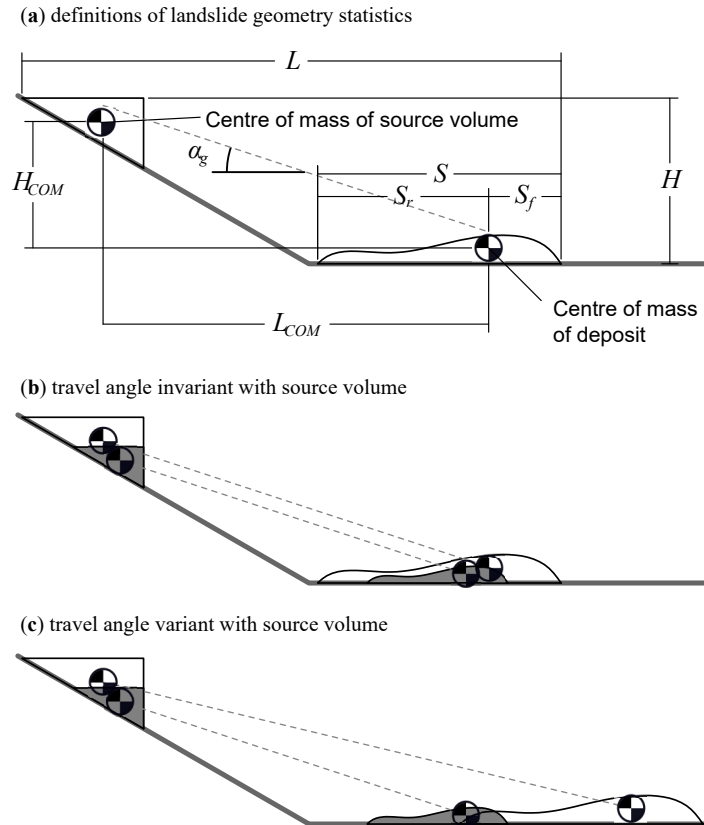


**Figure 1.** Schematic illustration of flows in a simple planar flume, showing (a) definition of geometry statistics, (b) the case where the travel angle  $\alpha_g$  is invariant with source volume, and (c) potential variation of  $\alpha_g$  with changing source volume indicating a variation within the rheology.

78 been associated with an apparent friction coefficient (e.g. [Parez & Aharonov, 2015](#)). Con-  
79 ceptually, the travel angle may be invariant with source volume ([Figure 1b](#)), or it may  
80 vary with the source volume ([Figure 1c](#)) where scale effects are significant. Aggregated  
81 observations of historical debris flows, compiled by [Corominas \(1996\)](#) and [Rickenmann](#)  
82 ([2011](#)), illustrate the general trend of decreasing travel angle (signifying increased mo-  
83 bility and a decrease in effective flow resistance) as source volume increases. While there  
84 is a lack of consensus in the literature, collisionality (e.g. [Armanini 2013](#)), fragmenta-  
85 tion (e.g. [Bowman et al. 2012](#); [Caballero et al. 2014](#)), pore pressure diffusion length-scales  
86 (e.g. [Iverson 2015](#); [Kaitna et al. 2016](#)), and thermal effects (e.g. [Voight & Faust 1982](#);  
87 [Goren & Aharonov 2007](#); [Alonso et al. 2016](#); [Fischer et al. 2018](#)) amongst other hypothe-  
88 ses (e.g. effects at the laboratory scale such as side wall effects and air drag; [Bryant et](#)  
89 [al. 2015](#); [Kessler et al. 2020](#)) have been investigated as potential mechanisms through  
90 which larger volume landslides achieve higher mobility.

91 Experimental flume flows using dry granular material have shown that when the rheol-  
92 ogy of the flow is very simple, the runout behavior can be straightforwardly related to  
93 general physical parameters like slope angle, basal friction and grain size (e.g. [Mangeney](#)  
94 [et al. 2010](#)) or predicted (e.g. [Bryant et al. 2015](#)). Flows on fully saturated or initially  
95 saturated materials have shown rheological changes with source volume (e.g. [de Haas](#)  
96 [et al. 2015](#)), fines content or moisture content (e.g. [Kaitna et al. 2014](#); [Hürlimann et al.](#)  
97 [2015](#); [Zhou et al. 2018](#)).

98 Numerical simulations of landslide runout offer the ability to release a source volume,  
99 propagate its flow over a 2D or 3D geometrical representation of the terrain, and pro-  
100 vide estimates of inundation depth, velocity, and definition of the maximum distal reach  
101 of the debris for a given pairing of rheology and rheological parameters. Rheological mod-  
102 els are chosen based on the nature of the flow; in particular, to account for the effect of  
103 pore fluid. With the addition of an interstitial fluid to a granular flow, particles are sub-  
104 ject to both buoyancy and drag forces ([Armanini, 2013](#); [Iverson, 1997](#)). For a frictional  
105 continuum material, particle buoyancy serves to reduce the effective weight of the par-  
106 ticles, leading to reduced effective stress, and shear resistance, and hence, heightened mo-  
107 bility of the debris. In frequently used flow resistance models (e.g. simple friction or [Voellmy](#)  
108 [model](#), in which a turbulence term is added to the frictional model to tune flow veloc-  
109 ity), pore pressure is considered implicitly. For a fully liquefied or low solids content flow,  
110 the effect of interstitial fluid may be more conveniently modelled as an equivalent fluid  
111 defined by a viscosity and yield strength (e.g. [Bingham](#) or [Herschel-Bulkley](#) rheology)  
112 for the duration of the flow. In both cases, pore pressure effects are typically considered  
113 to be constant during the duration of the flow. The validity of this assumption has been  
114 explored in [Tayyebi et al. \(2021\)](#), who suggest model choice should be guided through  
115 a consideration of two competing characteristic times: i) consolidation time and ii) prop-  
116 agation time. For scenarios in which the time of pore pressure dissipation is rapid in com-  
117 parison to the travel time, the high permeability debris is unlikely to retain excess pos-  
118 itive pore pressure, permitting simpler models of pore pressure effects to be used. On  
119 the other hand, it may be appropriate for fully undrained models to simulate lower per-  
120 meability flows, such as high water content slurries or liquefied debris. Debris flows with  
121 intermediate permeability between these two end members have the most computationally  
122 complex requirements for numerical simulation as the consolidation time and travel  
123 time can be of the same order.

124 The addition of an interstitial fluid is therefore recognized to have a dominant impact  
125 on the mobility of the flow. However, experimental studies in which both the bulk-scale  
126 (runout) and grain-scale behaviour of identical granular material in a dry and saturated  
127 initial state are directly compared are rare. If such a study were to be performed, it would  
128 provide a unique opportunity to test numerical simulation outcomes by first constrain-  
129 ing the frictional properties of the material (i.e. matching the runout behaviour of the  
130 dry experiments of different source volumes) before independently evaluating the imple-  
131 mentation of rheological models to account for buoyancy, fluid drag, and pore pressure

132 affecting the frictional material. The relative contributions of each mechanism may be  
133 revealed by matching the volume scaling effects.

134 In this manuscript we focus on the end member cases of high permeability debris which  
135 is initially dry or initially saturated with the objective of defining the influence of inter-  
136 stitial fluid and landslide volume on the runout distance and the relative contributions  
137 of translation and spreading in a material in which excess pore pressure is not expected  
138 to occur. A monodisperse material was used to ensure no segregation of particle size would  
139 take place during flow which could alter the rheologic behaviour, other than that caused  
140 by variation in solid and fluid concentration. Granular material was selected of a large  
141 enough grain size to isolate the effects of buoyancy and drag on the flows and allow for  
142 particle-level observation of contact behaviour and flow regimes. Dry flows of the iden-  
143 tical source volumes were also tested as a direct point of reference for comparison.

144 In the remainder of the manuscript, we first describe the research flume, instrumenta-  
145 tion, and high speed video analysis methods used for the experiments. The flow regimes  
146 of both dry and initially saturated  $0.8 \text{ m}^3$  flows are then described and illustrated us-  
147 ing representative frames and depth profiles. Next, velocity and volume fraction results  
148 are presented from the range of source volumes ( $0.2$  to  $1.0 \text{ m}^3$ ) to illustrate the varia-  
149 tion in regimes. Finally, laser scanning results of the deposit morphology of each trial  
150 are used to explore the nature of the relationship between travel angle and source vol-  
151 ume for both dry and wet flows.

## 152 **2 Experimental Setup & Methodology**

153 The experiments used a large indoor testing facility (Figure 2) and high speed imagery  
154 to investigate the mechanisms that lead to increased mobility when water is added to  
155 granular flows. The  $2.09 \text{ m}$  wide flume features a  $8.23 \text{ m}$  long section inclined  $30^\circ$  from  
156 horizontal and a  $33 \text{ m}$  long horizontal runout section. For the entirety of the inclined  
157 portion and for the first  $3.68 \text{ m}$  of the horizontal runout section, the base of the flume  
158 is constructed from bare aluminum and the side walls of the flume are glass to permit  
159 observation of the flows. Further down the flume, the base is constructed from smooth  
160 concrete. At the top, a release box with a hinged door can accommodate over  $1.0 \text{ m}^3$  of  
161 saturated material. The door was rapidly opened using pneumatic cylinders to initiate  
162 the experiment, with the door moving clear of the material within  $0.4 \text{ s}$ . At the com-  
163 pletion of the test, the final deposit shape was surveyed using a Faro Focus S 150 Light  
164 Detection and Ranging (LiDAR) scanner from two or more scanning positions.

### 165 **2.1 Video Capture & Instrumentation**

166 During the test, a Phantom v2512 high-speed camera was located near the end of the  
167 inclined portion of the flume (indicated as ‘CAM1’ on Figure 2) to capture mature flow  
168 behaviour in the travel stage. The camera was oriented in a side-on configuration to ob-  
169 serve through the transparent glass side walls, rotated such that the width of the image  
170 was parallel to the base of the flume. The high-speed camera was set to capture a  $1280$   
171  $\times 800$  pixel greyscale image at a frame rate of  $7,500 - 10,000 \text{ fps}$  (frames per second). A  
172 Tokina  $100 \text{ mm f}/2.8$  Macro lens was used at its widest aperture to limit the depth of  
173 field and distinguish only the particles next to the glass side walls. The field of view was  
174 approximately  $220 \text{ mm}$  by  $136 \text{ mm}$ . A typical particle of  $3.85 \text{ mm}$  diameter was repre-  
175 sented by a  $23$  pixel width in the resulting image.

176 Two initially saturated flows ( $0.4$  and  $0.8 \text{ m}^3$  source volumes) were repeated with the same  
177 high-speed camera and lens situated within the horizontal portion of the flume (‘CAM2’  
178 on Figure 2). At this location, the camera was situated further back from the sidewall.  
179 The field of view was approximately  $285$  by  $178 \text{ mm}$ , with a typical particle represented  
180 by  $17$  pixels.

181 Nine fluid pressure transducer sensors were installed into the base of the flume to quan-  
182 tify the basal fluid pressure (Figure 2). The sensors (TE Connectivity model U5244-000002-

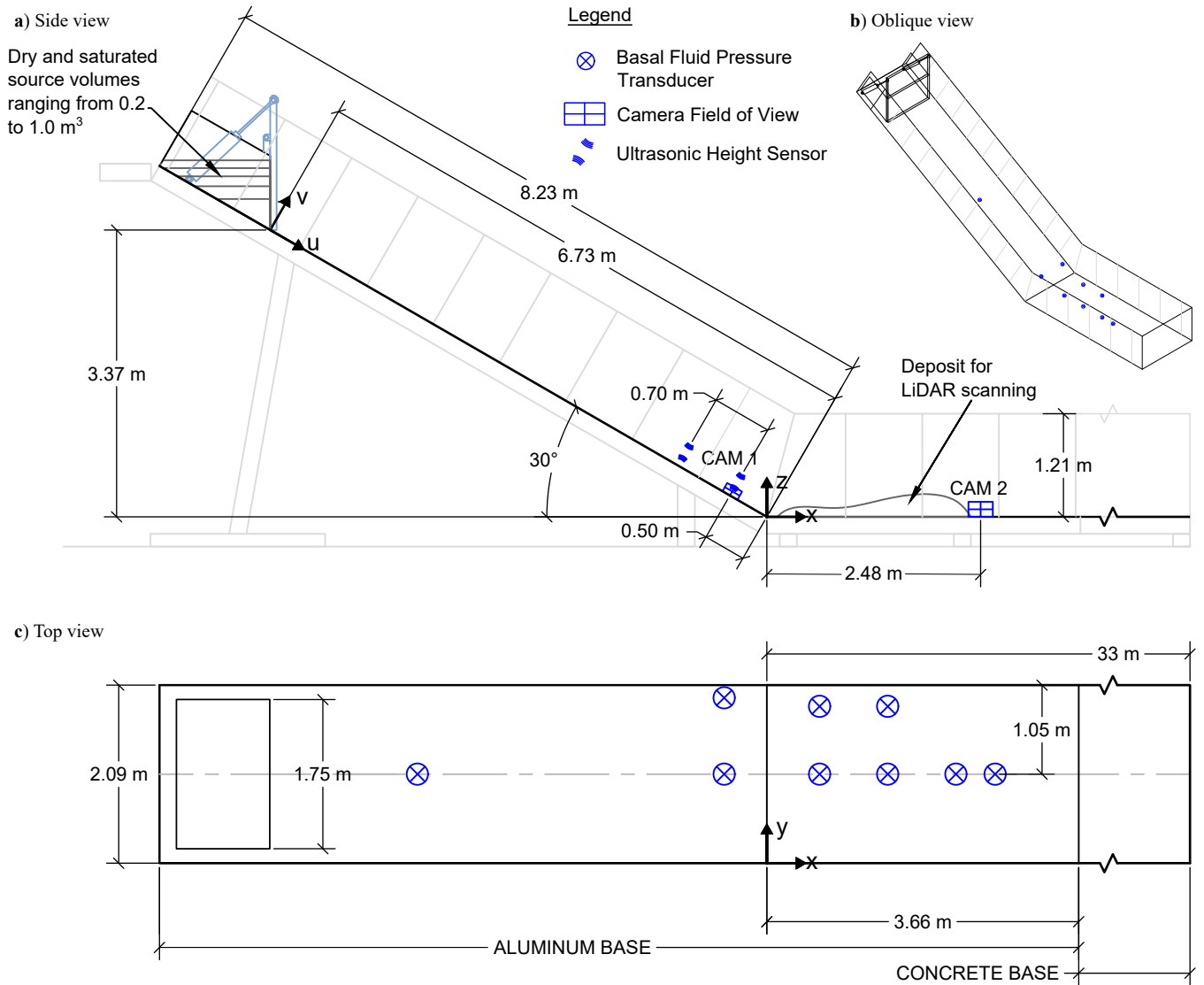


**Figure 2.** Diagram of (a) side profile, (b) oblique view, (c) top view of the experimental flume, illustrating the locations of high-speed camera fields of view, basal fluid pressure transducers, and ultrasonic height sensors.

183 14BG, 0 to 140 mbar range, manufacturer’s stated accuracy 7 mm, total error band 18  
 184 mm) were threaded directly into the flume. The fluid could enter each sensor through  
 185 seven holes of 2 mm diameter.

186 Two ultrasonic distance sensors (model S18UUAQ, Banner Engineering Corp., 2.5 ms  
 187 response time) were mounted above the inclined section of the flume, along the flume  
 188 centreline (Figure 2). These sensors recorded the flow height away from the influence of  
 189 the glass sidewalls by measuring the distance between the sensor and the top of the flow,  
 190 normal to the flume base.

191 The sensor signals were sampled and recorded at 2000 Hz. During the experiments, the  
 192 pressure sensors were subject to noise considered to be resonance of the flume. The nat-  
 193 ural frequency of the flume structure was measured at approximately 140 Hz. To coun-  
 194 teract this noise, the pressure sensor output signals were filtered using a 80 Hz low-pass  
 195 Butterworth filter.

## 196 2.2 Materials and Preparation

197 Pseudo-spherical ceramic beads, manufactured by Saint-Gobain Norpro and marketed  
 198 as Denstone 2000 Support Media, were used as the granular material for the experiments.  
 199 These beads were chosen for their pseudospherical shape, relatively uniform diameter,  
 200 and ability to be reused for multiple trials with minimal breakdown. The physical prop-  
 201 erties of a representative sample of 30 beads were measured and tabulated by Coombs  
 202 et al. (2019). The beads were found to have an average diameter of 3.85 mm, grain spheric-  
 203 ity of approximately 95%, and grain density of 2241 kg m<sup>-3</sup>. According to the manufac-  
 204 turer, the hardness of the beads exceeds 6.5 on the Mohs scale. Triaxial tests conducted  
 205 by Raymond (2002) gave effective friction angles of 33.7° at 20 kPa confining pressure.

206 The source volumes tested were comprised of 0.2, 0.4, 0.6, 0.8, and 1.0 m<sup>3</sup>. In each of  
 207 the dry and initially saturated states, the material was made level in the release box us-  
 208 ing a rake. In the initially saturated state, the pore spaces were inundated with water  
 209 but ponding water on top of the beads was minimized.

## 210 3 High-speed video analysis and calculated quantities

211 High-speed video was used to observe the flow structure and to provide images for fur-  
 212 ther analysis. In this section, we discuss the image analysis methods used to identify the  
 213 velocity and volume fraction for each test.

### 214 3.1 Particle displacement and velocity

215 The Particle Tracking Velocimetry (PTV) method involves first identifying the particle  
 216 locations in selected frames and then using a PTV algorithm to link individual particles  
 217 in successive frames (Brevis et al., 2010; Gollin et al., 2017; Taylor-Noonan et al., 2021).  
 218 In our experiments, the camera is oriented to match the inclination of the flume base to  
 219 optimise the field of view, e.g. so the particle movement vectors (Figure 3a) are gener-  
 220 ally horizontal in the illustrations. Thus, the direction of gravity is noted.

221 The images were analyzed in sets of fifty (50) images. Each set was initiated at an in-  
 222 terval of  $t = 0.05$  s during the passage of the flow. Within each set, the frames were  
 223 selected from the video such that the frames were  $\Delta t = .0004$  s apart (equivalent to  
 224 2,500 fps). For a particle moving at 5 metres per second, the movement was 11.5 pix-  
 225 els and the resulting ratio of particle movement per frame to particle diameter was 0.52.  
 226 For a particle moving at 1 metre per second, the corresponding movement was 2.3 pix-  
 227 els. The results were grouped into bins to prepare depth profiles of the quantities, each  
 228 drawn parallel to the flume base with height equal to one average particle diameter. Each  
 229 vector was decomposed into components parallel and perpendicular to the flume base.  
 230 Velocity profiles (Figure 3b) were calculated by averaging the components of each vec-  
 231 tor located within the bin, for all pairs of frames that comprise the set. The velocity of  
 232 the lowest bin, adjacent to the flume base, was considered to be the basal slip velocity.

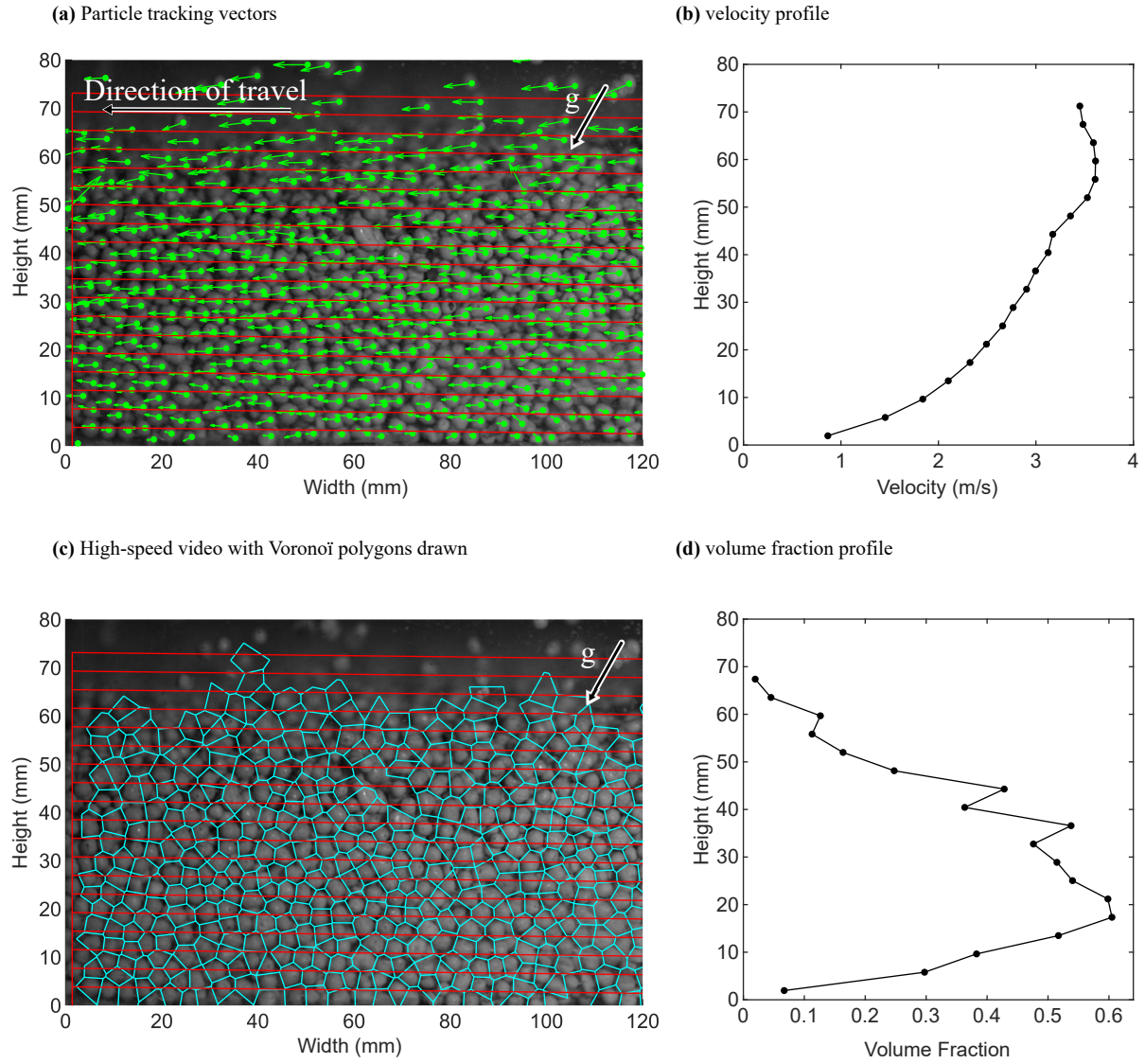


**Figure 3.** Representative video analysis and calculated profiles using PTV for  $0.8 \text{ m}^3$  dry flow at peak flow height, illustrating (a) displacement vectors identified by PTV within bins drawn parallel to flume base (in red), (b) velocity profile calculated from displacement vectors within each bin, (c) Voronoï polygons drawn around particle locations for use in volume fraction estimation method, and (d) estimated volume fraction profile.

### 233 3.2 Volume Fraction

234 The volume fraction  $\nu$  was estimated using the method proposed by Capart et al. (2002),  
 235 which considers the size and shape of Voronoï polygons drawn around the identified par-  
 236 ticle locations as the basis of estimation. The image plane is divided into regions, each  
 237 containing one identified particle centroid location (Figure 3c). The regions are drawn  
 238 such that all points in the region are closer to that identified particle than any other.

239 This method uses a roundness parameter  $\xi = 4\pi A/P^2$  where A and P are the area and  
 240 perimeter of the Voronoï polygon around the particle, respectively. The roundness pa-  
 241 rameter  $\xi$  is calculated for all the particles in a bin over all the frames in each set. Voronoï  
 242 polygons which share an edge with the analysis area of interest were disregarded, as the  
 243 shape of these polygons may have been ‘clipped’ by the analysis area of interest. Before  
 244 inclusion into the average, each Voronoï polygon was assessed for size and shape; Voronoï  
 245 polygons with areas exceeding 2.5 times the area of an average particle or with a round-  
 246 ness parameter  $\xi$  below 0.70 were then discarded. Any polygon bordering a polygon which  
 247 was discarded due to size or shape was not included in the average.

248 The volume fraction profile (Figure 3d) is estimated by:

$$249 \nu = \frac{\nu}{\nu_{rcp} = \left( \frac{\xi - \xi_0}{\xi_{rcp} - \xi_0} \right)^\beta} (1)$$

250 where indices “rcp” and “0” designate the state of random close packing and the dilute  
 251 state, respectively. For random close packing of spheres,  $\nu_{rcp} \approx 0.64$  (Allen & Thomas,  
 252 1999). Capart et al. (2002) performed a calibration study for volume fractions in the range  
 253  $0.20 \leq \nu \leq 0.55$  and found calibration constants  $\xi_{rcp} = 0.84$ ,  $\xi_0 = 0.72$ , and  $\beta = 3.5$ .  
 254 This method was developed for the case where particles are observed against a rigid trans-  
 255 parent wall, but calibrated with the average volume fraction in the cell. Thus, the method  
 256 is expected to estimate the volume fraction away from the influence of the rigid wall.

257 For the purposes of further analysis and discussion in this paper, the flow height of the  
 258 trials was set by the threshold,  $\nu = 0.20$ , over height and time (Figure 4). Some man-  
 259 ual adjustments were made to exclude particles which were not immediately beside the  
 260 sidewall glass. The top of fluid was manually marked on images at 0.05 second intervals  
 261 for the wet flows.

## 262 4 Flow characteristics

263 We begin the comparison of dry and saturated flows through visual observations of flow  
 264 structure, velocity, volume fraction, and pore pressure measured at the observation point  
 265 near the end of the inclined section of the flume (the ‘CAM1’ location). The 0.8 m<sup>3</sup> vol-  
 266 ume is chosen for this comparison of typical anatomy of the flows, with the variability  
 267 observed in larger and smaller volumes and full analysis of the resulting deposit morphol-  
 268 ogy explored in future sections of the manuscript.

### 269 4.1 Dry flow

270 The flow regimes within a 0.8 m<sup>3</sup> dry flow are revealed by the velocity and volume frac-  
 271 tion profiles as it passes the ‘CAM1’ location (Figure 5) at selected times  $t$  since door  
 272 opening. The initial front of the debris flow is heralded by dilute, saltating particles (Fig-  
 273 ure 5a) with a (basal) slip velocity in excess of 2.5 ms<sup>-1</sup>. A high level of collisional ac-  
 274 tivity is seen when reviewing the video. The transition from collisional regime to fric-  
 275 tional regime begins with a global reduction in speed. As the core approaches (Figure 5b),  
 276 the volume fraction increases to approximately 0.32. The bottom of the flow slows due  
 277 to friction with the base and the shear rate  $\dot{\gamma}$  quickly increases. The slip velocity at  $t =$   
 278 1.74 s is 1.8 ms<sup>-1</sup>, while the surface velocity is 4.0 ms<sup>-1</sup> with a flow height of 36 mm.

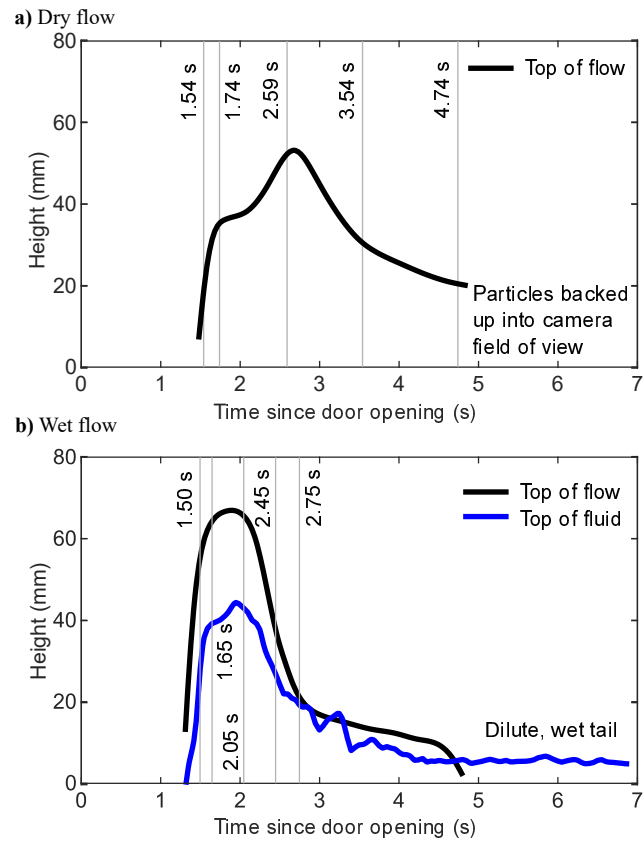


**Figure 4.** Flow heights vs time, at ‘CAM1’ location near the end of the inclined section of flume, for representative  $0.8 \text{ m}^3$  (a) dry and (b) wet flows. The initially saturated flow is taller, has the majority of the mass biased towards the front of the flow, and has a long thin tail portion. The top of fluid is below the top of flow at the time of peak flow height.

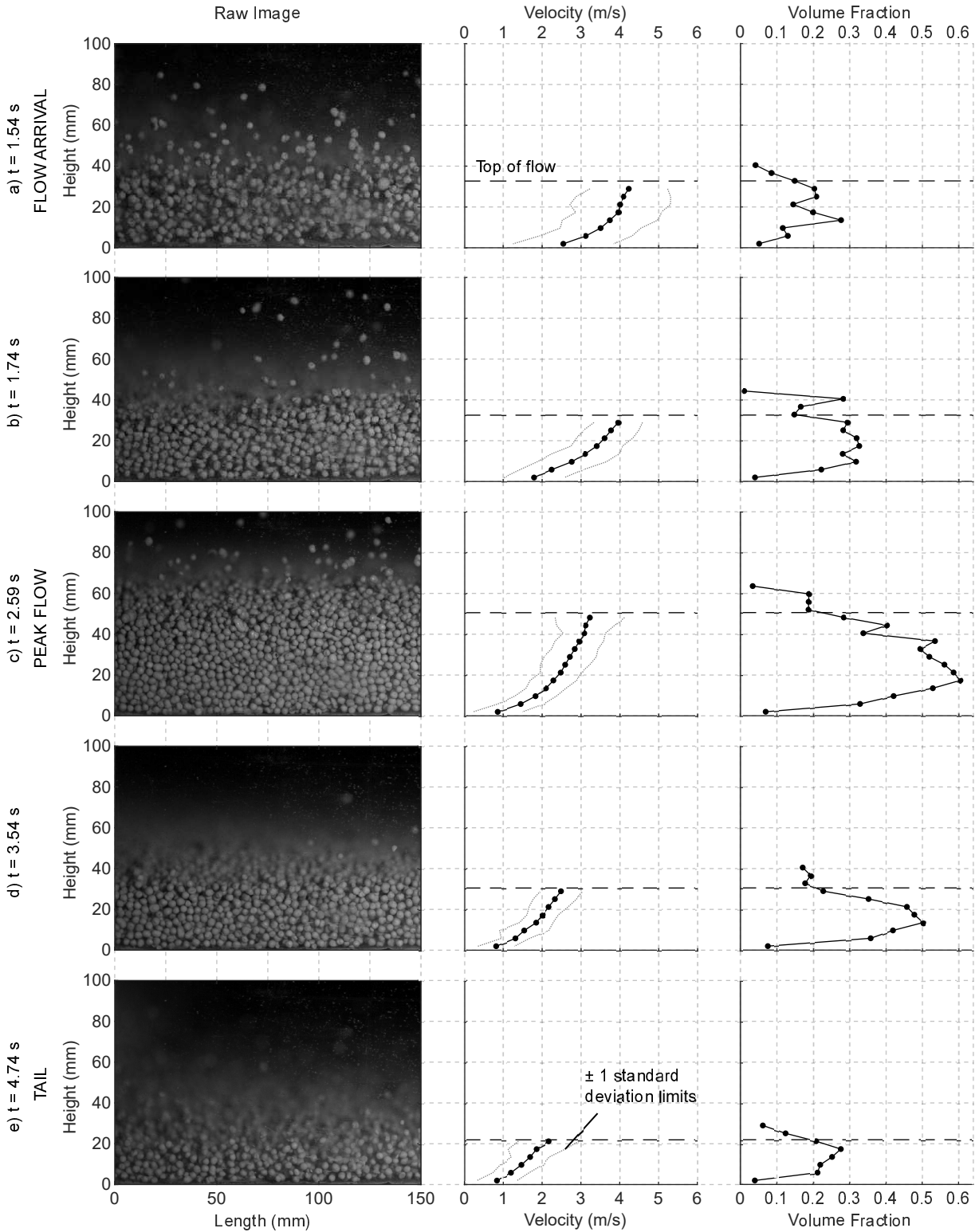


**Figure 5.** Anatomy of 0.8 m<sup>3</sup> dry flow at end of inclined section of flume (‘CAM1’), showing a frame of video, the velocity profile with  $\pm 1$  standard deviation limits (in the 0.02 s observation time window), and the volume fraction  $\nu$  at times (a)  $t = 1.54$  s, (b)  $t = 1.74$  s, (c)  $t = 2.59$  s, (d)  $t = 3.54$  s, (e)  $t = 4.74$  s since door opening.

279 The peak flow height comprises a dense frictional core above a collisional base with a higher  
 280 shear rate. The peak flow height of approximately 52 mm is visible at  $t = 2.59$  s (Fig-  
 281 ure 5c). The volume fraction  $\nu$  exceeds the ‘dense’ threshold of 0.49 (Jenkins, 2007) for  
 282 the height interval between 16 and 39 mm in the core of the flow. The surface velocity  
 283 is approximately  $3.4 \text{ ms}^{-1}$ , slower than at  $t = 1.74$  s even though the flow height is higher.  
 284 The slip velocity has reduced further to approximately  $0.9 \text{ ms}^{-1}$ .

285 The volume fraction reduces gradually and the pressure at the base reduces after the body  
 286 of the flow passes (Figure 5d). At  $t = 3.54$  s,  $\nu$  ranges up to a maximum of 0.51. At  
 287  $t = 4.74$  s (Figure 5e), the flow height has reduced to approximately 21 mm and  $\nu$  has  
 288 reduced to approximately 0.28. The slip velocity remains at  $0.8 \text{ ms}^{-1}$  and the surface  
 289 velocity has reduced to  $2.2 \text{ ms}^{-1}$ . At  $t = 4.85$  s, the determination of the velocity for  
 290 the  $0.8 \text{ m}^3$  flow is not possible as particles at rest begin to back up into the camera’s field  
 291 of view. The runout morphology for this experiment is discussed in Section 6.

## 292 4.2 Saturated source volume

293 The typical behaviour of a fluid saturated flow is presented in Figure 6 for the  $0.8 \text{ m}^3$   
 294 volume. The partitioning into a head section, frictional core, collisional base, and tail  
 295 section is more pronounced for a wet flow than dry flow of the same volume. The front  
 296 of the flow arrives before the fluid, similar to the unsaturated granular front observed  
 297 in laboratory experiments by Leonardi et al. (2015) and Turnbull et al. (2015). In the  
 298 early arrival stages of the core of the flow (Figure 6a), the top of fluid is seen at an ap-  
 299 proximate height of 30 mm while the flow height is approximately 43 mm. The free sur-  
 300 face velocity exceeds  $4.8 \text{ ms}^{-1}$ , faster than the dry flow. The velocity profile shows a very  
 301 high shear rate of approximately  $200 \text{ s}^{-1}$  near the flume base and minimal shear rate above  
 302 the top of fluid. The flow is dilute, with identified volume fractions typically ranging be-  
 303 tween 0.3 and 0.4.

304 By  $t = 2.05$  s, the flow height and the top of fluid are at their peak (Figure 6c), while  
 305 the surface velocity has decreased to  $4.5 \text{ ms}^{-1}$ . The concentration of shear near the base  
 306 of the flow continues. The density is less than the dry flow and is further reduced near  
 307 the top of flow. Below the top of fluid, the maximum volume fraction,  $\nu = 0.52$ . In the  
 308 portion of the flow above this,  $\nu = 0.21$ .

309 The top of fluid is coincident with the surface at  $t = 2.75$  s (Figure 6e) and the tail of  
 310 the flow is in view. The flow is dilute with  $\nu = 0.32$ . The slip velocity reduces from  $1.6 \text{ ms}^{-1}$   
 311 at  $t = 2.75$  s to  $0.4 \text{ ms}^{-1}$  at  $t = 4.00$  s, at which time the flow is only two particles  
 312 high. This is in stark contrast to the tail end of the dry flows, where the slip velocity is  
 313 seen to increase.

314 A similar, repeat, test was carried out for the  $0.8 \text{ m}^3$  initially saturated flow, with the  
 315 high speed camera set at the ‘CAM2’ location (Figure 2) on the horizontal runout por-  
 316 tion of the flume. The results show that the flow arrives in a dense state at the resid-  
 317 ual water content with a free surface speed of approximately  $2.6 \text{ ms}^{-1}$  (Figure 7a), which  
 318 is approximately half that at the time of peak flow at the upstream ‘CAM1’ position.  
 319 The peak flow height is over 100 mm, approximately two-thirds greater than at ‘CAM1’.  
 320 This shows that the material has laterally compressed following the change in slope. Shear-  
 321 ing is concentrated near the base. The volume fraction generally exceeds  $\nu = 0.5$  through-  
 322 out the flow.

323 The top of fluid rises quickly to 102 mm above the flume base at  $t = 2.40$  s (Figure 7b).  
 324 A reduction in the volume fraction occurs simultaneously, especially near the top of the  
 325 flow. As the core passes and the tail comes into view at  $t = 3.00$  s (Figure 7c), the ve-  
 326 locity decreases throughout the depth profile. The density increases in the lower portion  
 327 of the flow. Later, the flow arrests completely while the tail is in the view of the cam-  
 328 era.

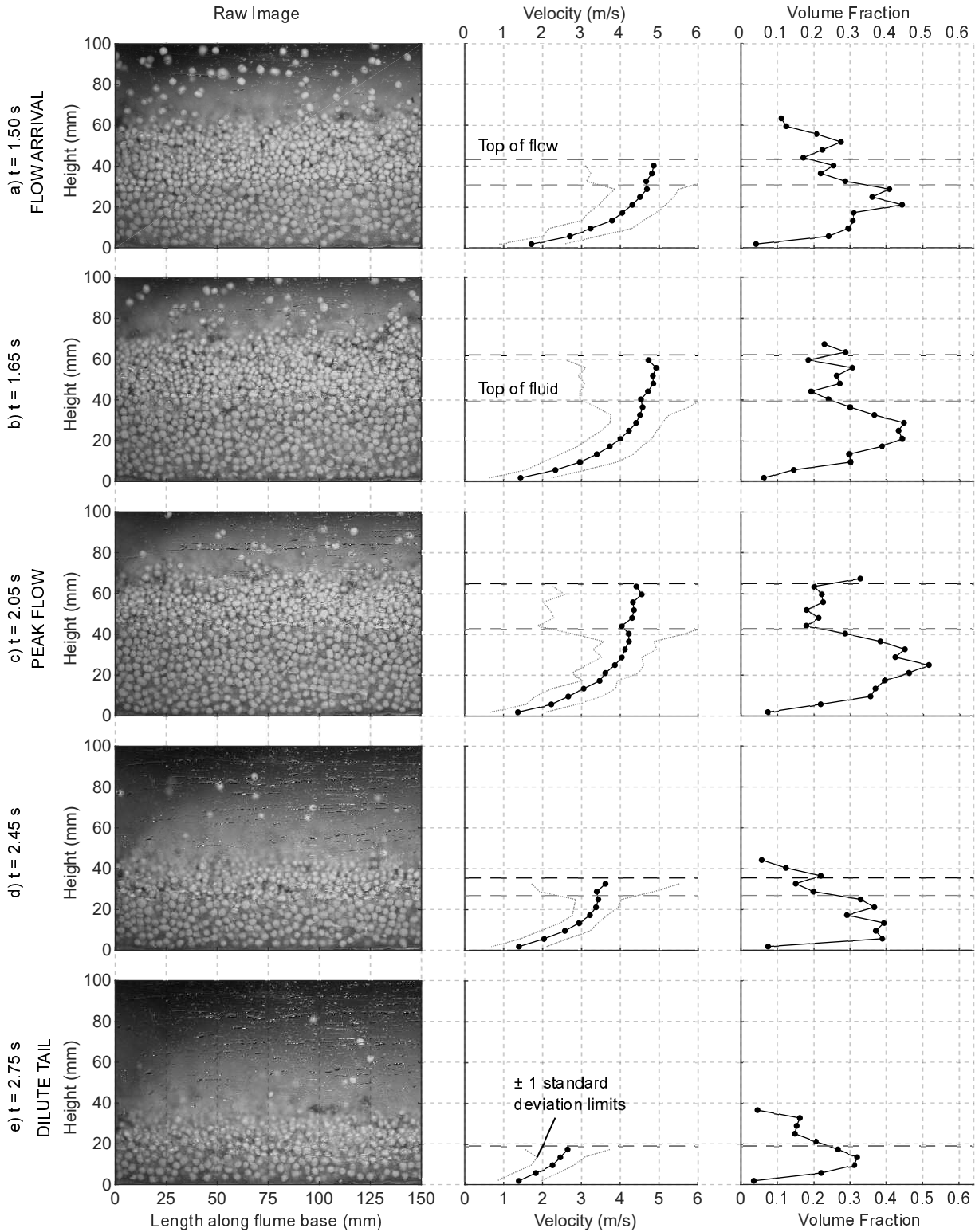


**Figure 6.** Anatomy of  $0.8 \text{ m}^3$  initially saturated flow at end of inclined section of flume ('CAM1') showing a frame of video, the velocity profile with  $\pm 1$  standard deviation limits (in the  $0.02 \text{ s}$  observation time window), and the volume fraction  $\nu$  at times (a)  $t = 1.50 \text{ s}$ , (b)  $t = 1.65 \text{ s}$ , (c)  $t = 2.05 \text{ s}$ , (d)  $t = 2.45 \text{ s}$ , (e)  $t = 2.75 \text{ s}$  since door opening.

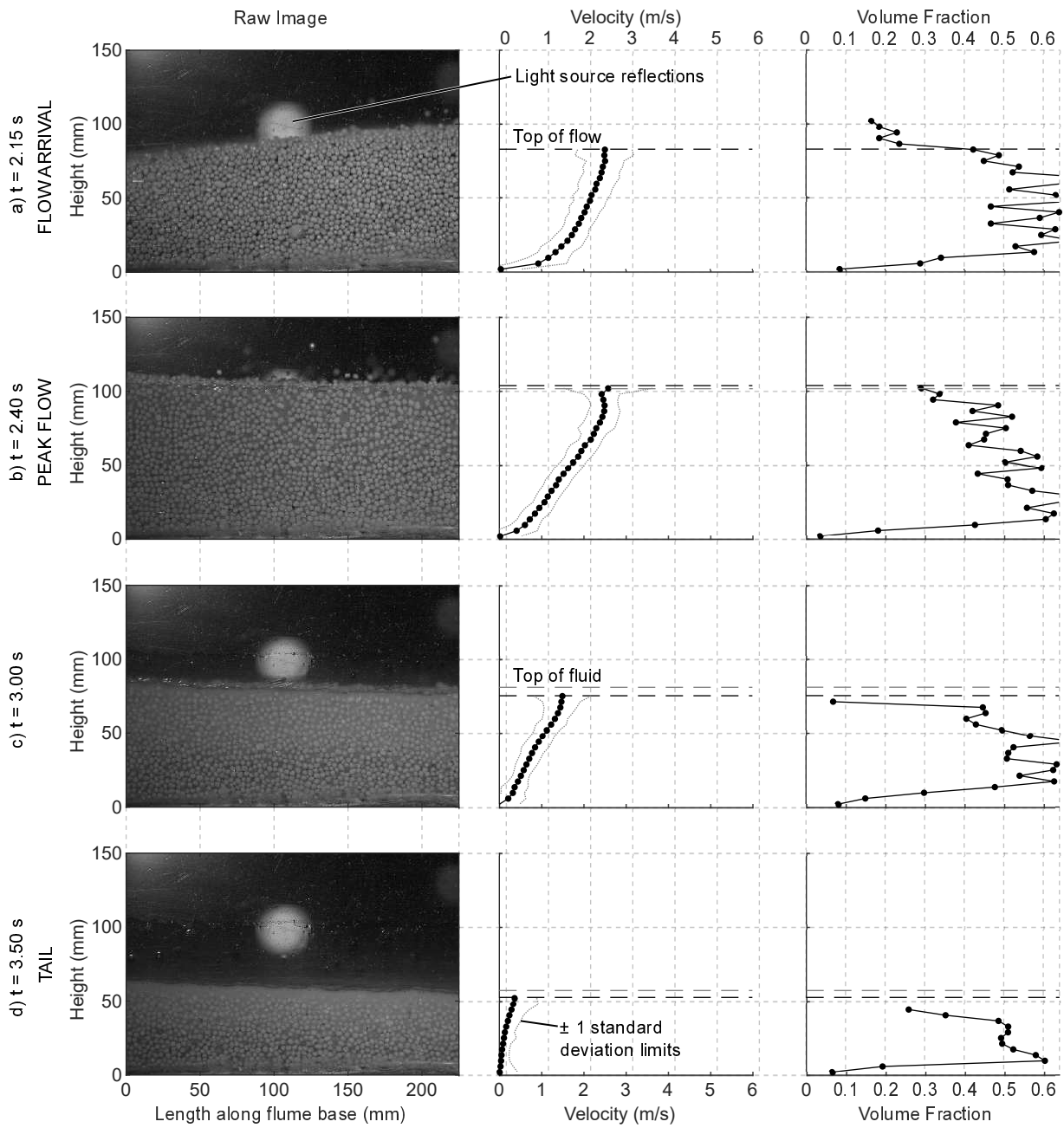


**Figure 7.** Anatomy of  $0.8 \text{ m}^3$  wet flow in horizontal runout section of flume ('CAM2') showing a frame of video, the velocity profile with  $\pm 1$  standard deviation limits (in the 0.02 s observation time window), and the volume fraction  $\nu$  at times (a)  $t = 2.15$  s, (b)  $t = 2.40$  s, (c)  $t = 3.00$  s, (d)  $t = 3.50$  s since door opening.

### 329 4.3 Basal fluid pressures

330 During the initially saturated 0.8 m<sup>3</sup> flow, the two laterally separated basal fluid pres-  
 331 sure sensors on the inclined portion of the flume measure show similar peak pressure mea-  
 332 surements. This leads to the conclusion that the flow is sufficiently mature at ‘CAM1’  
 333 to have recovered from the initial impulse of the granular collapse from the source box.  
 334 The pressure traces from the centreline location to the side location at  $x = +1.42$  m  
 335 are also generally similar. When comparing the visually-identified flow height to the re-  
 336 sults of the ultrasonic flow height sensor, good agreement is seen between the centre and  
 337 sides of the flow.

338 The visually-identified top of fluid at the side of the flow can be compared to the mea-  
 339 sured basal fluid pressure  $P$  at the centre of the flow, expressed as an equivalent bed-  
 340 normal fluid height  $H = P/\rho_w g \cos \theta$ , where the density of water  $\rho_w = 1000 \text{ kg} \cdot \text{m}^3$ ,  
 341 the slope angle  $\theta = 30^\circ$  and  $g = 9.81 \text{ m} \cdot \text{s}^{-2}$ . The equivalent height of the basal fluid  
 342 pressure is equal to the the height of the fluid, indicating that the matrix fluid pressures  
 343 did not exceed the equivalent hydrostatic regime.

344 The basal fluid pressures consistently increase across the four sensors situated on the hor-  
 345 izontal runout portion. The highest pressures observed are at the furthest distance from  
 346 the release box. This is attributed to the increasing flow height as the front of the flow  
 347 slows and the rear of the flow cascades over. Good agreement is seen between the equiv-  
 348 alent fluid height from the sensor at  $x = +2.68$  m and the top of fluid. The wet flow  
 349 is subject to contraction during the arrest phase but the basal fluid pressures do not in-  
 350 crease above hydrostatic.

## 351 5 Effect of varying source volume

352 In this section, we expand on the comparison of dry and initially saturated flows using  
 353 observations of flow thickness, velocity, volume fraction, and pore pressure measured at  
 354 the observation point near the end of the inclined section of the flume (the ‘CAM1’ lo-  
 355 cation) for source volumes ranging between 0.2 to 1.0 m<sup>3</sup>. This comparison is conducted  
 356 to look at grain-scale mechanisms controlling the flow structure that may give rise to scale  
 357 effects with flow volume.

### 358 5.1 Flow thicknesses and fluid pressures

359 As source volume increased through the tested range of 0.2 to 1.0 m<sup>3</sup>, the observed max-  
 360 imum flow thickness at  $x = -0.50$  m (‘CAM1’) increased from 38 to 51 mm for the dry  
 361 flows and from 30 to 79 mm for the initially saturated flows.

362 As shown in Figure 8 at  $x = -0.50$  m, the maximum equivalent bed-normal fluid height  
 363 (as calculated in Section 4.3) is equal to the peak flow height for the range of initially  
 364 saturated source volumes tested. This suggests the matrix fluid pressures did not exceed  
 365 the equivalent hydrostatic regime. The pore pressure ratio  $r_u$ , defined here as the ratio  
 366 of fluid pressure to the total vertical pressure, ranges between [0.36 : 0.44].

### 367 5.2 Behaviour at peak flow height

368 In Figure 9, the time of peak flow height passing ‘CAM1’ is selected as a basis for com-  
 369 parison between the flows. This is the time when the flow is at its thickest and most dense  
 370 state, and therefore the transport rate of mass is highest. A review of the profiles, dis-  
 371 cussed in detail below, provides information on the state of flow at the end of the incline  
 372 as well as the partitioning of particles between highly shearing, lightly shearing, and col-  
 373 lisional regimes.

374 At the time of peak flow height passing ‘CAM1’, the velocity profile of each of the ini-  
 375 tially saturated flows (“wet”) is faster than that of the dry flows. The overall velocity of  
 376 the wet flows increases as source volume increases, with the top of the core of the 1.0 m<sup>3</sup>

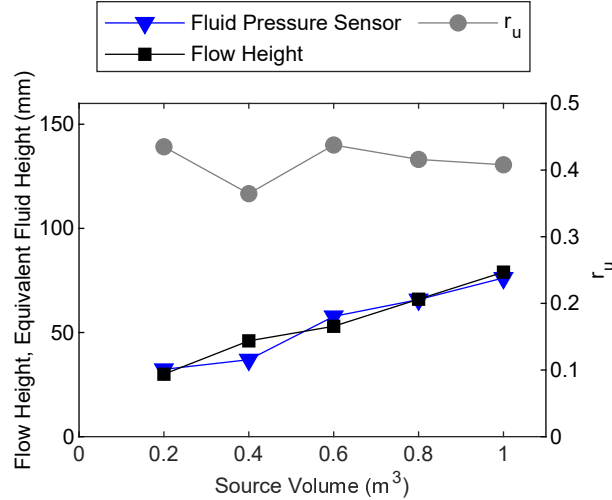


**Figure 8.** Maximum flow thicknesses and fluid pressures observed at  $x = -0.50$  m along centreline for initially saturated trials, with equivalent fluid height remaining below flow height over range of source volumes tested. The pore pressure ratio  $r_u$  is defined here as the ratio of fluid pressure to the total vertical pressure.

377 flow attaining a speed exceeding  $5.0 \text{ ms}^{-1}$ . Wet flows of all volumes are each seen to have  
 378 a very high shear rate near the base of the flow. The opposite is noted for the dry flows,  
 379 which are seen to be slower for each height in the flow as source volume increases.

380 At ‘CAM2’ after the change in slope, the  $0.8 \text{ m}^3$  wet flow maintains this highly shear-  
 381 ing flow which transports material (at residual water content) to the front of the flow.  
 382 By comparison, the  $0.4 \text{ m}^3$  wet flow displays minimal shearing at the same location.

383 Across the range of source volumes, the volume fraction profiles at the time of peak height  
 384 passing ‘CAM1’ (Figure 9) for the dry flows display a similar shape as the  $0.8 \text{ m}^3$  flow  
 385 discussed above. The maximum volume fraction of the core increases with source vol-  
 386 ume. Each volume of wet flows displays a similar shape as the  $0.8 \text{ m}^3$  flow, with a re-  
 387 duction in volume fraction above the top of fluid. The  $0.2$  through  $0.6 \text{ m}^3$  dry flows each  
 388 are entirely in a collisional regime when assessed by volume fraction. The  $0.8$  and  $1.0 \text{ m}^3$   
 389 dry flows each have portions exceeding  $\nu = 0.583$ , indicating a frictional regime. While  
 390 the maximum volume fractions of the wet flows increase slightly with source volume, the  
 391 wet flows each have a lower maximum volume fraction than the dry flows of the same  
 392 source volume and all remain in a collisional regime. For the dry flows, the volume frac-  
 393 tion near the base is relatively consistent over the range of  $0.2$  to  $0.8 \text{ m}^3$ . For the  $1.0 \text{ m}^3$   
 394 flow, the dense region is seen to extend down to near the flume base, suggesting that the  
 395 increased confining pressure of the thicker frictional core has suppressed the collisional  
 396 base. The wet flows displayed a reduction in volume fraction near the base over the range  
 397 of source volumes, coincident with a high shear rate.

### 398 5.3 Longitudinal distribution of regimes

399 Following the finding that the core region of the initially saturated flows appears to enter  
 400 an efficient mode of transport that increases in velocity with flow thickness, the size  
 401 of this core region relative to the total flow size is examined here. The partitioning into  
 402 regimes along the length of the flow from head to tail can be assessed through plots of  
 403 the measured quantities for each analysis interval and depth bin. Figure 10 shows the  
 404 volume fraction results and Figure 11 shows the velocity results in a contour plot for-

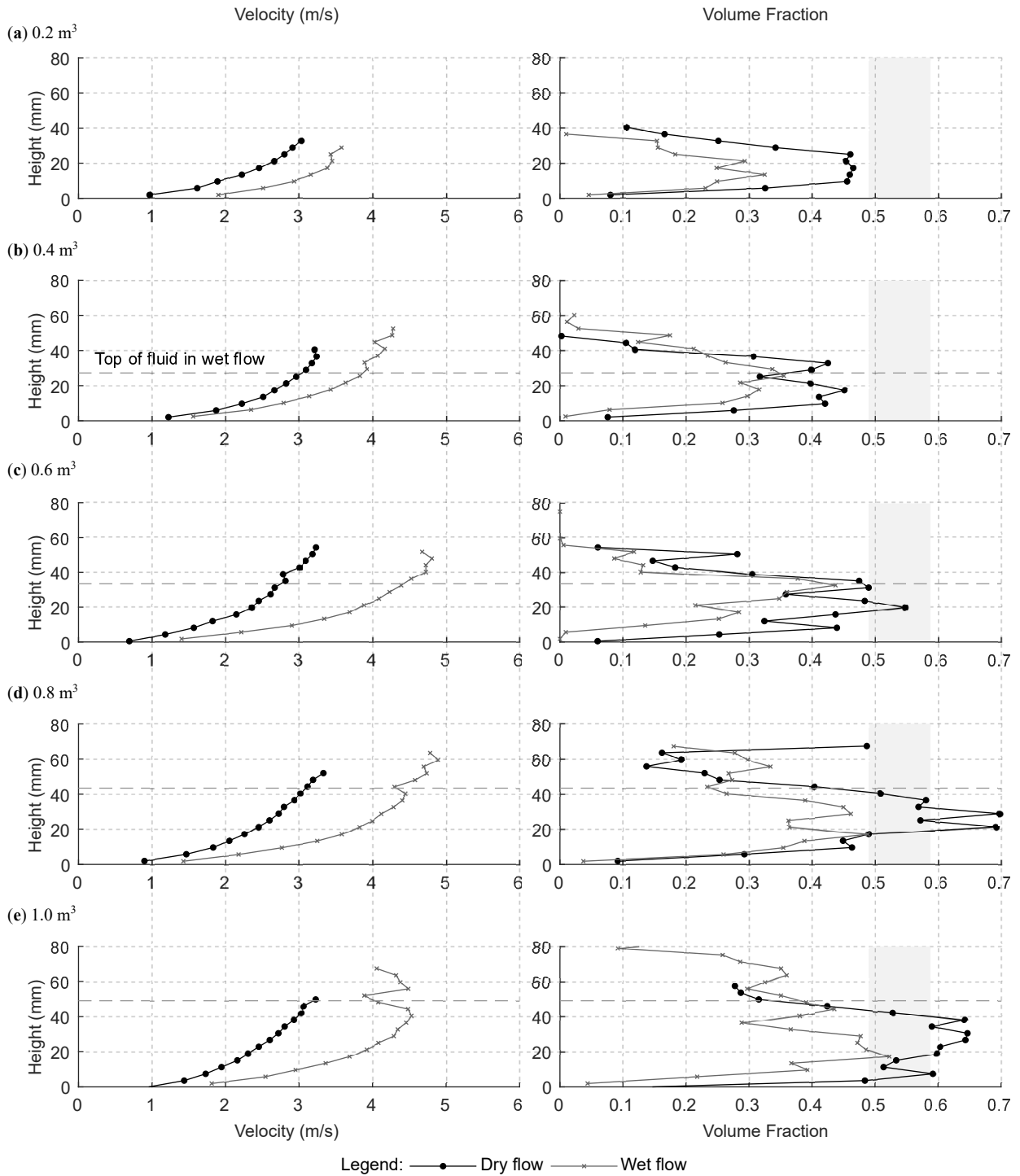


**Figure 9.** Comparison of depth profiles of streamwise velocity and volume fraction at the time of maximum flow height for (a)  $0.2 \text{ m}^3$  to (e)  $1.0 \text{ m}^3$  flows in  $0.2 \text{ m}^3$  increments. The shading in the volume fraction plot represents the dense collisional regime ( $0.49 \leq \nu \leq 0.583$ ).

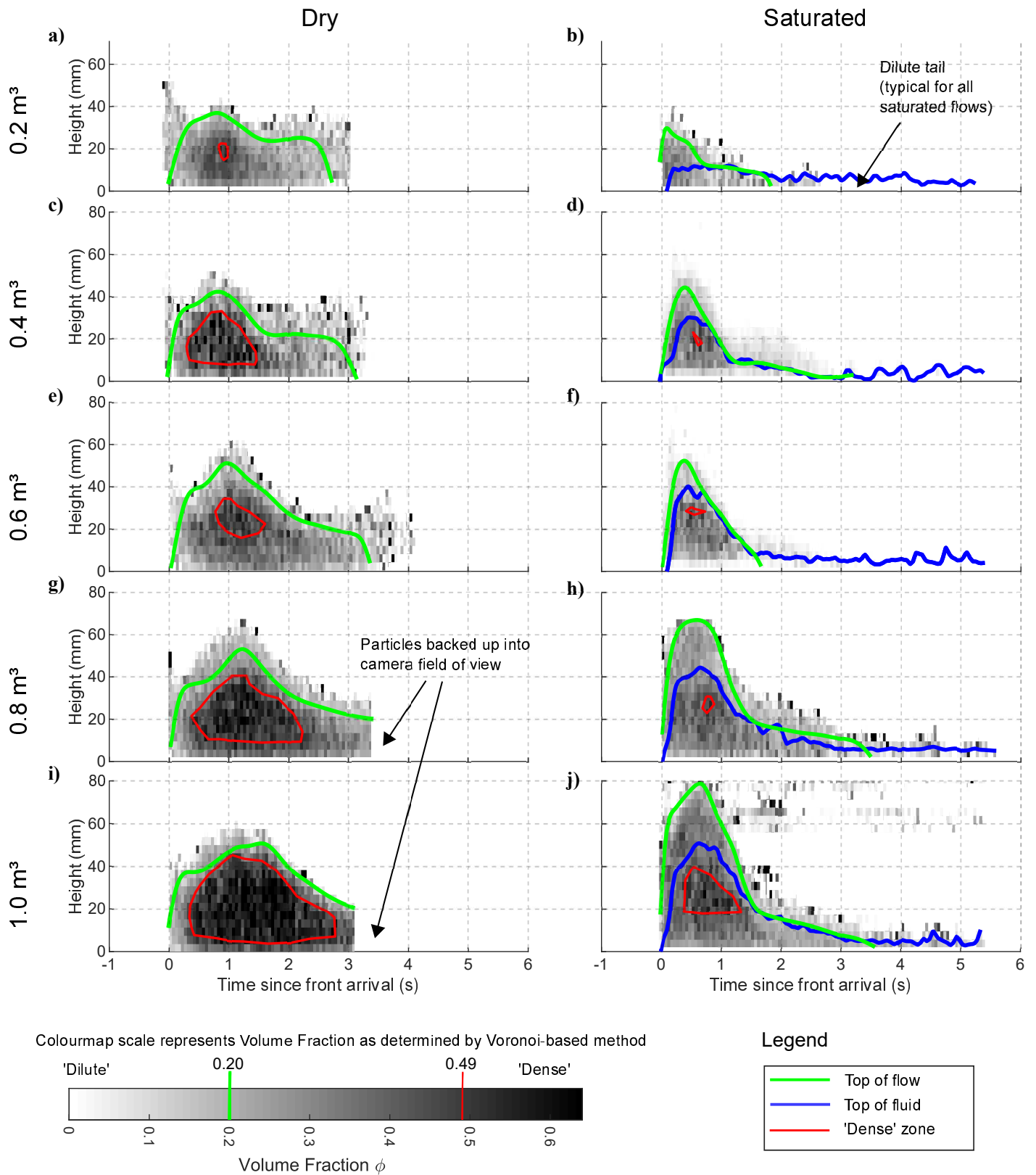


**Figure 10.** Height (y)-Time (x)-Volume Fraction (color scale) plots for for dry and saturated trials over the range of source volumes, illustrating the formation of a dense granular core for dry flows and a comparatively dilute core for wet flows. Both flows exhibit a reduction in volume fraction near the rigid flume base.

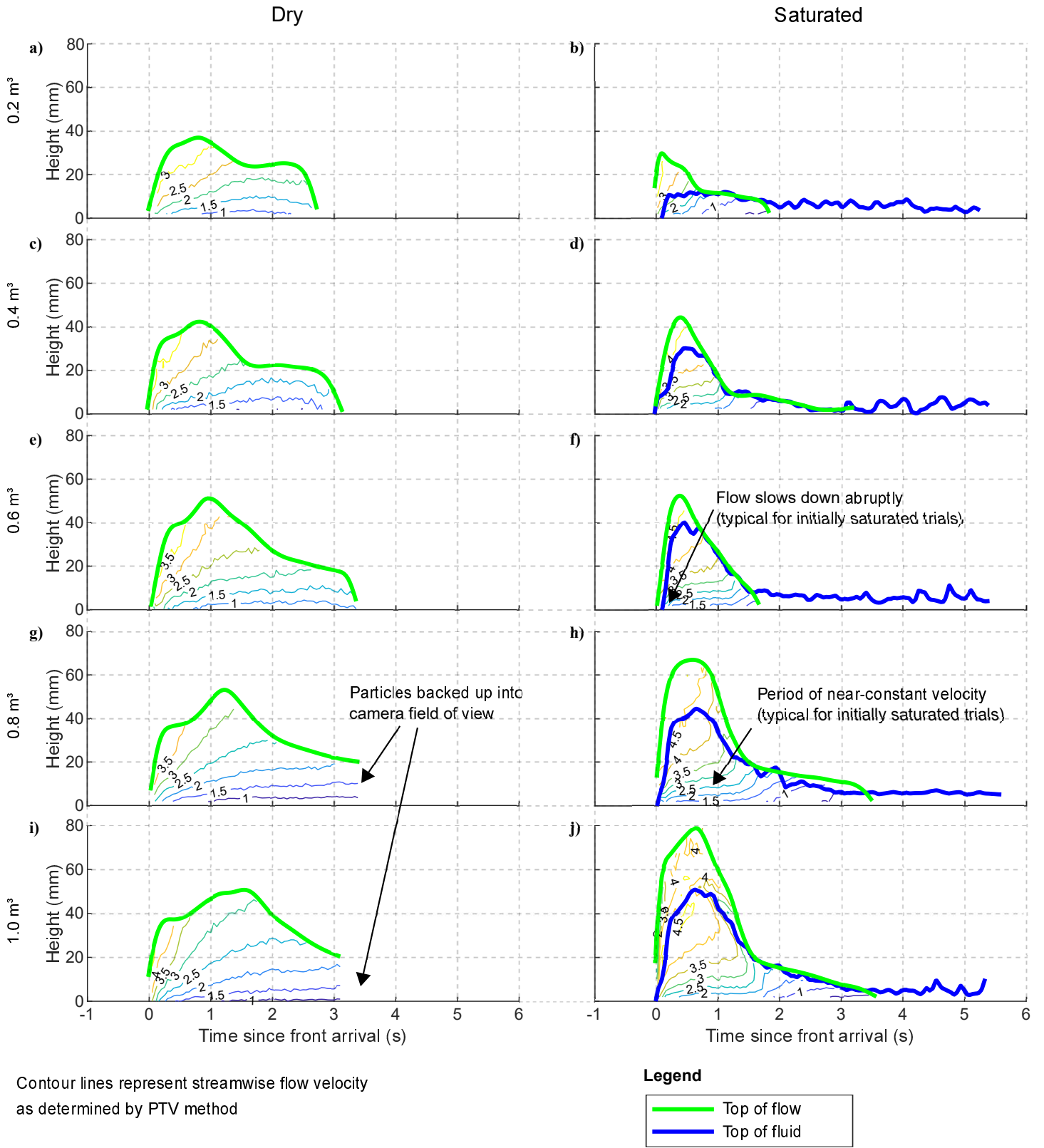


**Figure 11.** Height (y)-Time (x)-Velocity (color scale) plots for dry and initially saturated trials over the range of source volumes, illustrating the period of near-constant velocity near the base of the flume for the initially saturated state, suggesting that the flows find a ‘most efficient state’ for translation.

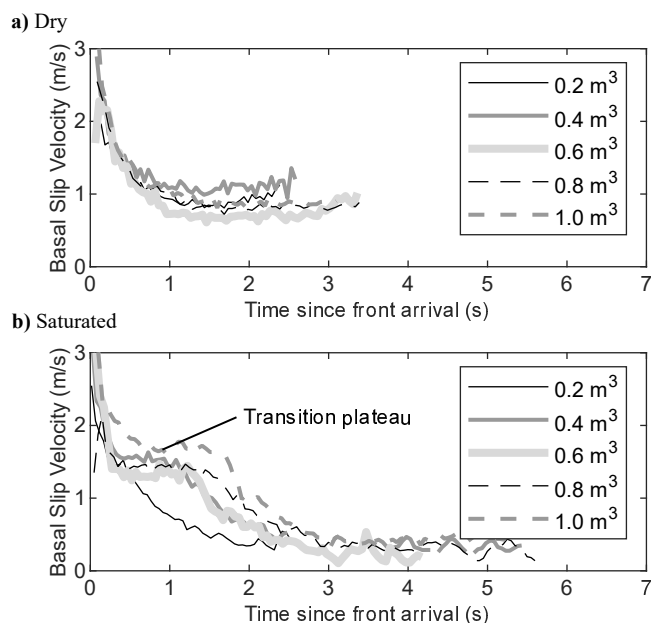


**Figure 12.** Comparison of basal slip velocities at end of incline for (a) dry trials illustrating the gradual decline in basal slip velocity and (b) initially saturated trials, illustrating a ‘step’ phenomenon where the velocity remains constant while the core passes, then quickly reduces to a slow speed ( $<0.5\text{ ms}^{-1}$ ) for the tail.

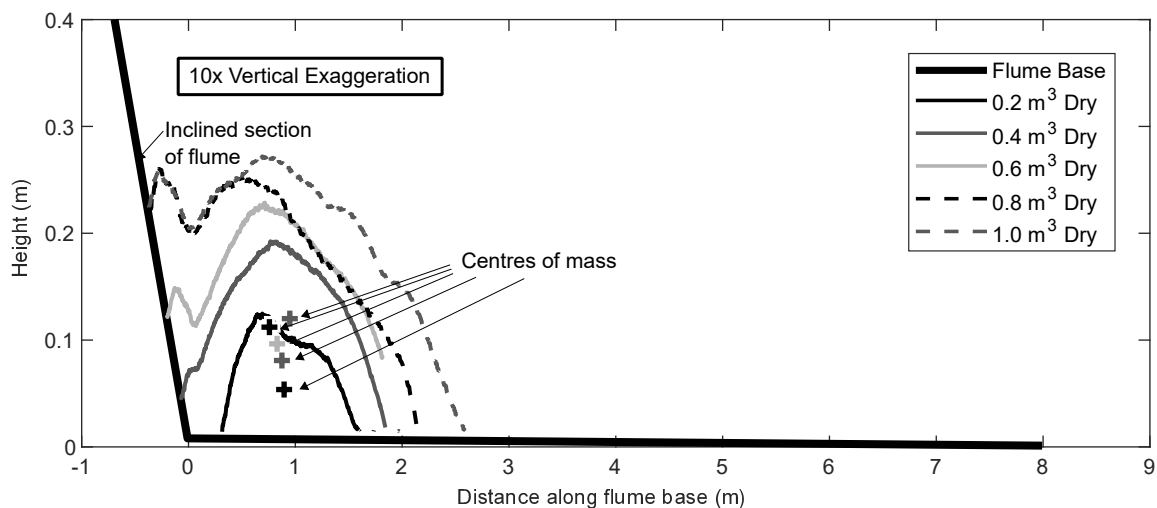
405 mat where the contour lines represent isovelocity lines. The shear rate can be inferred  
 406 from the vertical distance between the isovelocity contour lines: isovelocity lines closer  
 407 together represent a higher shear rate. Where the lines are parallel to the x-axis, that  
 408 portion of the velocity profile is constant with time.

409 The volume fraction of the dry flows (Figure 10) shows partitioning of the flow into a  
 410 dilute, saltating head preceding the front, a dense core where volume fraction increases  
 411 with source volume, and a gradual of reduction of volume fraction towards the tail. Dur-  
 412 ing this transition period, the velocity results show only gradual changes with time (Fig-  
 413 ure 11). Geometric similarity of the flow height over time is evident across the range of  
 414 source volumes and the change in flow height between core and tail is gradual. In con-  
 415 trast, Figure 10 shows the saltating head is minimal to non-existent for the wet flows,  
 416 while the regime of the tail is distinct from the core for both volume fraction and veloc-  
 417 ity (Figure 10 and Figure 11, respectively).

418 The initially saturated flows each display a period with near-constant velocity in the base  
 419 of the flow (Figure 11), with the duration of this increasing with source volume. Only  
 420 a short period of near-constant velocity in the base is observed within the  $0.2\text{ m}^3$  flow,  
 421 increasing to 0.9 s for the  $1.0\text{ m}^3$  flow. The maximum shear rate near the base does not  
 422 vary significantly with source volume, suggesting that the wet flows find and remain in  
 423 a ‘most efficient’ state. This phenomenon is also visible on a plot of the slip velocity over  
 424 time from the flow front (Figure 12) as a distinct plateau for the wet flows but not for  
 425 the dry flows.

426 The wet flows slowed down significantly from core to tail in contrast with the dry flows,  
 427 which slowed down less significantly. An effect for the deceleration of the wet flows is thought  
 428 to be due to surface tension between the liquid phase with the flume base and sidewalls.  
 429 At this stage, the tail portions of the initially saturated flows are slow moving and of low

(a) Dry trials



(b) Initially saturated trials

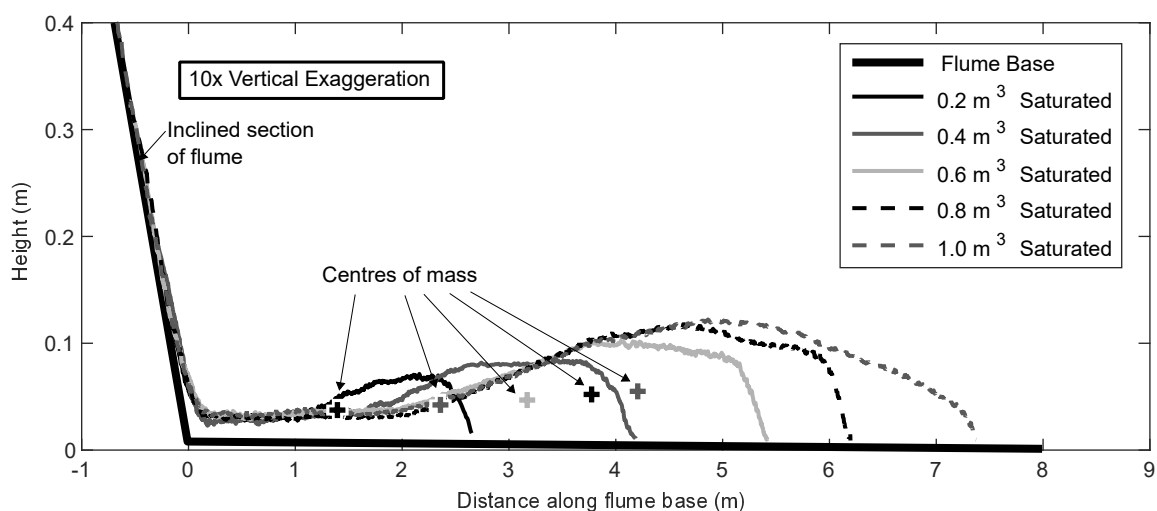


**Figure 13.** Comparison of resultant deposit morphology profiles for (a) dry and (b) initially saturated trials, with calculated centres of mass indicated.

430 volume fraction and minimal thickness. Some ceramic beads remained on the flume sur-  
 431 face at the end of the experiments until the remnant water evaporated. The material par-  
 432 titioned to this slow-moving tail would reduce the volume available to be transported  
 433 at high speed in the core section of the flow. This is in accordance with the description  
 434 of ‘starving’ avalanches by Bartelt et al. (2007).

## 435 6 Variation of morphology of resultant deposit with source volume

436 The observations of grain-scale phenomena clearly illustrate that the granular flow struc-  
 437 tures evolve with volume, and more so for the wet than dry flows. In this section, we ex-  
 438 plore the consequences of these differences in grain scale behaviour, as seen in the de-  
 439 posit morphology.

440 The deposit morphology for each of the five dry and five saturated flow volumes, cap-  
 441 tured using LIDAR scanning, is presented in Figure 13. The profile of deposit morphol-

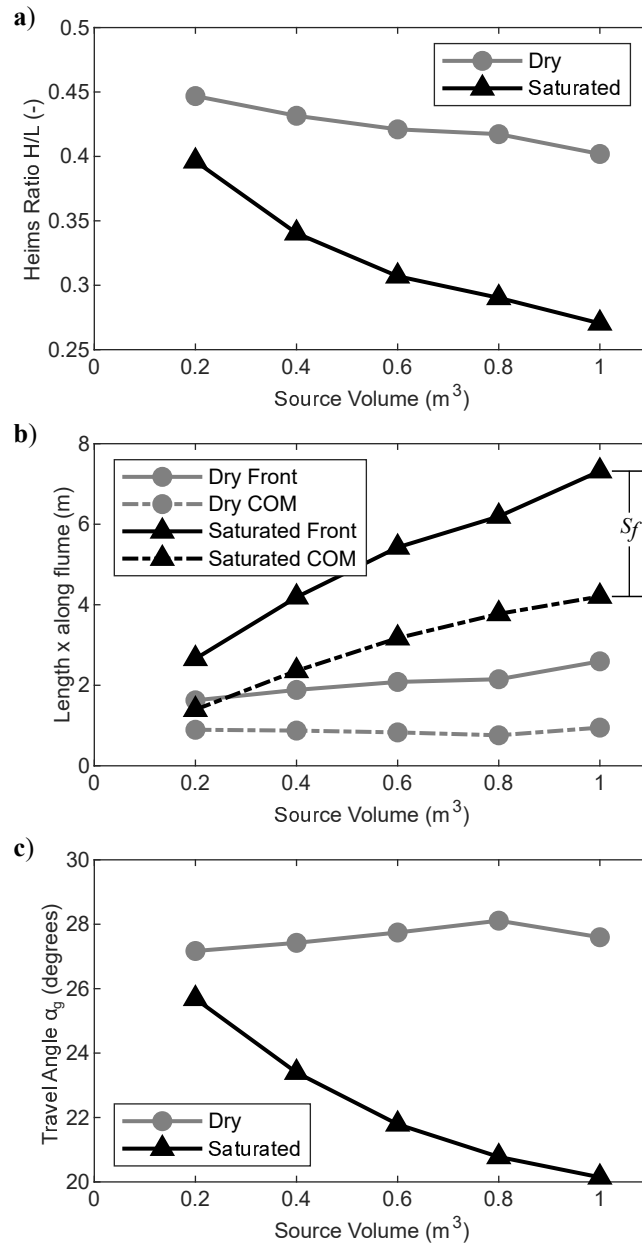


**Figure 14.** Comparison of summary statistics of mobility, showing (a) Heim's ratio from top of source volume to distal reach of deposit, (b) position of front extent of deposit and centre-of-mass of deposit, illustrating the relative contributions of each to total runout, and (c) travel angle between centres of mass.

ogy illustrates geometrical similarity over the range of source volumes for dry flows, in agreement with the model postulated by Parez & Aharonov (2015). In contrast, the initially saturated flows display markedly increased runout distances as source volume increases. Runout statistics, illustrated schematically in Figure 1a, can be used to summarize the resultant deposit morphologies (Figure 14). The frontal extents of the flow are considered in Heim's Ratio  $H/L$  (Figure 14a). Heim's Ratio remains relatively constant for dry flows but decreases significantly for initially saturated flows, indicating increased mobility with volume. The forward spread  $S_f$  of the deposit is the distance between the the centre-of-mass and front extent of the deposits (Figure 14b). A slight increase in the forward spreading distance is seen for dry flows, commensurate with geometric similitude. For the initially saturated flows, a much larger increase of the forward spreading distance with volume occurs, the majority of which is from translation of the centre-of-mass.

The travel angle statistics summarize the translation of the centre-of-mass (Figure 14c), with a lower travel angle indicating a general increase in mobility. For the dry tests, a relatively consistent travel angle of  $27.1^\circ$  to  $28.1^\circ$  was calculated over the range of source volumes tested. For the wet tests, the travel angle reduced significantly from  $25.7^\circ$  for a source volume of  $0.2 \text{ m}^3$  to  $20.1^\circ$  for a source volume of  $1.0 \text{ m}^3$ . This marked decrease indicates that one or more physical processes within the rheology of the wet flows are affected by experiment size.

## 7 Conclusions

A series of monodisperse granular flows was released within a large laboratory flume to define the effect of landslide volume on the runout distance and the relative contributions of translation and spreading in a material in which excess pore pressure is not expected to occur. Both dry and initially saturated states were tested and the source volume was systematically varied from  $0.2$  to  $1.0 \text{ m}^3$  in  $0.2 \text{ m}^3$  increments. The use of high permeability debris retained the possible influences of particle buoyancy and fluid drag but was confirmed to not result in basal fluid pressures that exceed hydrostatic conditions. The tests exhibited marked differences in runout distance and flow regimes as observed by high-speed video between dry and initially water saturated conditions.

The dry flows were heralded by a region of saltating particles, followed by a dense, frictional core, the density and extent of which increased with source volume. The velocity quickly slowed as the frictional core arrived. Through the range of source volumes, it was observed that the velocity at the time of peak flow height was highest for the smallest source volume and lowest for the largest source volume, throughout the flow depths. The particle velocity was then seen to increase after the passage of the core.

Distinct regimes were seen within the initially saturated flows, with differentiation not only from the head to tail of the flow but also with flow depth. The front of each of the initially saturated flows was comprised of particles at residual water content, which had broken free of the fluid matrix. At the time of peak flow height, the velocities of the initially saturated flows were each faster than that of the dry flows and were generally faster as source volume increased. The top of fluid was below the top of the flow at the time of peak flow height indicating that a significant mass of particles was transported at residual water content, at high speed. The density of the core of the initially saturated flows also increased with source volume, but was lower than the dry flows of the same source volume.

The initially saturated flows each demonstrated a period of near-constant velocity with high shear rates near the base of the flows. This is interpreted to be a 'most efficient' flow regime. The length of this period increased with source volume. After the core of the flows passed, the flow velocities rapidly decreased to rates lower than observed in the dry flows, presumably due to surface tension between water and the flume.

493 The consequences of these differences in grain-scale interaction can be quantified through  
 494 an assessment of the resulting deposit morphology and the relative contributions of trans-  
 495 lation and spreading to the total runout length. For the dry flows, the travel angle in-  
 496 creased very slightly from 27.1° to 28.1° (indicating slightly decreased mobility) for larger  
 497 source volumes of dry material. This suggests that the effective friction at the base in-  
 498 creased with the denser frictional cores due to increased confining pressure. For wet flows,  
 499 the mobility increased significantly from 25.7° to 20.1° as source volume increased. This  
 500 increase in total mobility was seen to come more from translation of the centre-of-mass  
 501 than spreading at the front. This confirms that significant scaling effects are present within  
 502 multiphase granular flows, even without the presence of ‘excess’ pore pressures. The ex-  
 503 perimental data suggests that this is, in part, due to the partitioning of the source vol-  
 504 ume into a highly shearing base and a slow tail section. The remainder of the source vol-  
 505 ume is transported very quickly above the base, and is the prime contributor to the long  
 506 runout distances observed. The experiments demonstrate that even with a coarse gran-  
 507 ular material, the effects of the interstitial fluid and partitioning into flow regimes can  
 508 lead to scaling effects as flow thickness varies. This data provides additional support to  
 509 the conclusion that flume size matters, particularly for fluid saturated flows. The crit-  
 510 ical processes within multiphase granular flows are complex and localized, and physical  
 511 experiments linking particulate behaviour to bulk response are required to fully validate  
 512 and calibrate conceptual and numerical models.

513 This study begins to address the paucity of such experiments through the publication  
 514 of a unique dataset that combines the detailed grain-scale visual observations of flow struc-  
 515 ture, velocity, and volume fraction, with the observed consequences in terms of effective  
 516 friction and debris spreading. This unique dataset is publicly available on the Scholar-  
 517 sportal Dataverse repository to serve as a well-defined test scenario to assess the role of  
 518 interstitial fluid in numerical runout models of debris flows.

## 519 Open Research

520 The data used in this research are archived in the Queen’s University Dataverse (<https://dataverse.scholarsportal>).  
 521 A Dataverse entry will be created for the dry and saturated granular flows and made ac-  
 522 cessible at a DOI at manuscript acceptance.

## 523 Acknowledgments

524 This project is the result of a Leverhulme Trust International Network Grant (#IN-2016-  
 525 041) “The Rosetta Stone Network: Physical testing towards a common understanding  
 526 of debris flows”. Funding for the first author provided by a NSERC Discovery Grant to  
 527 the last author. The first author would like to thank Natalie Arpin, Branna MacDougall,  
 528 Erica Treflik-Body, Megan McKellar, Andrea Walsh, Artur Sass Braga, Joshua Cogh-  
 529 lan, Graeme Boyd, Hal Stephens and Richard Foley for their ideas and assistance in the  
 530 laboratory.

## 531 References

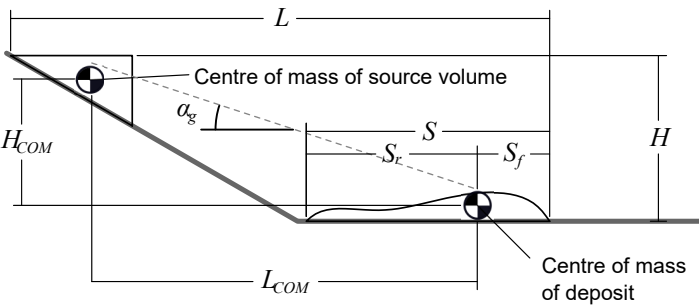
- 532 Allen, S. M., & Thomas, E. L. (1999). *The structure of materials* (Vol. 44). Wiley  
 533 New York.
- 534 Alonso, E. E., Zervos, A., & Pinyol, N. M. (2016). Thermo-poro-mechanical anal-  
 535 ysis of landslides: from creeping behaviour to catastrophic failure. *Géotechnique*,  
 536 *66*(3), 202–219. doi: 10.1680/jgeot.15.lm.006
- 537 Armanini, A. (2013). Granular flows driven by gravity. *Journal of Hydraulic Re-*  
 538 *search*, *51*(2), 111–120. doi: 10.1080/00221686.2013.788080
- 539 Bartelt, P., Buser, O., & Platzer, K. (2007). Starving avalanches: Frictional mech-  
 540 anisms at the tails of finite-sized mass movements. *Geophysical Research Letters*,  
 541 *34*(20). doi: 10.1029/2007gl031352

- 542 Bowman, E., Take, W., Rait, K., & Hann, C. (2012). Physical models of rock  
543 avalanche spreading behaviour with dynamic fragmentation. *Canadian Geotechni-*  
544 *cal Journal*, *49*(4), 460–476. doi: 10.1139/t2012-007
- 545 Brevis, W., Niño, Y., & Jirka, G. H. (2010). Integrating cross-correlation and relax-  
546 ation algorithms for particle tracking velocimetry. *Experiments in Fluids*, *50*(1),  
547 135–147. doi: 10.1007/s00348-010-0907-z
- 548 Bryant, S. K., Take, W. A., & Bowman, E. T. (2015). Observations of grain-scale  
549 interactions and simulation of dry granular flows in a large-scale flume. *Canadian*  
550 *Geotechnical Journal*, *52*(5), 638–655. doi: 10.1139/cgj-2013-0425
- 551 Caballero, L., Sarocchi, D., Soto, E., & Borselli, L. (2014). Rheological changes  
552 induced by clast fragmentation in debris flows. *Journal of Geophysical Research:*  
553 *Earth Surface*, *119*(9), 1800–1817. doi: 10.1002/2013jf002942
- 554 Capart, H., Young, D. L., & Zech, Y. (2002). Voronoï imaging methods for the mea-  
555 surement of granular flows. *Experiments in Fluids*, *32*(1), 121–135. doi: 10.1007/  
556 s003480200013
- 557 Coombs, S., Apostolov, A., Take, W. A., & Benoît, J. (2019). Mobility of dry granu-  
558 lar flows of varying collisional activity quantified by smart rock sensors. *Canadian*  
559 *Geotechnical Journal*. doi: 10.1139/cgj-2018-0278
- 560 Corominas, J. (1996). The angle of reach as a mobility index for small and large  
561 landslides. *Canadian Geotechnical Journal*, *33*(2), 260–271. doi: 10.1139/t96-005
- 562 Dade, W. B., & Huppert, H. E. (1998). Long-runout rockfalls. *Geology*, *26*(9), 803.  
563 doi: 10.1130/0091-7613(1998)026<0803:lrr>2.3.co;2
- 564 de Haas, T., Braat, L., Leuven, J. R. F. W., Lokhorst, I. R., & Kleinhans, M. G.  
565 (2015). Effects of debris flow composition on runout, depositional mechanisms,  
566 and deposit morphology in laboratory experiments. *Journal of Geophysical Re-*  
567 *search: Earth Surface*, *120*(9), 1949–1972. doi: 10.1002/2015jf003525
- 568 Fischer, J.-T., Kaitna, R., Heil, K., & Reiweger, I. (2018). The heat of the flow:  
569 Thermal equilibrium in gravitational mass flows. *Geophysical Research Letters*,  
570 *45*(20). doi: 10.1029/2018gl079585
- 571 Gollin, D., Brevis, W., Bowman, E. T., & Shepley, P. (2017). Performance of PIV  
572 and PTV for granular flow measurements. *Granular Matter*, *19*(3). doi: 10.1007/  
573 s10035-017-0730-9
- 574 Goren, L., & Aharonov, E. (2007). Long runout landslides: The role of frictional  
575 heating and hydraulic diffusivity. *Geophysical Research Letters*, *34*(7). doi: 10  
576 .1029/2006gl028895
- 577 Hürlimann, M., McArdell, B. W., & Rickli, C. (2015). Field and laboratory analysis  
578 of the runout characteristics of hillslope debris flows in switzerland. *Geomorphol-*  
579 *ogy*, *232*, 20–32. doi: 10.1016/j.geomorph.2014.11.030
- 580 Iverson, R. M. (1997). The physics of debris flows. *Reviews of Geophysics*, *35*(3),  
581 245–296. doi: 10.1029/97rg00426
- 582 Iverson, R. M. (2015). Scaling and design of landslide and debris-flow experiments.  
583 *Geomorphology*, *244*, 9–20. doi: 10.1016/j.geomorph.2015.02.033
- 584 Jenkins, J. T. (2007). Dense inclined flows of inelastic spheres. *Granular Matter*,  
585 *10*(1), 47–52. doi: 10.1007/s10035-007-0057-z
- 586 Kaitna, R., Dietrich, W. E., & Hsu, L. (2014). Surface slopes, velocity profiles and  
587 fluid pressure in coarse-grained debris flows saturated with water and mud. *Jour-*  
588 *nal of Fluid Mechanics*, *741*, 377–403. doi: 10.1017/jfm.2013.675
- 589 Kaitna, R., Palucis, M. C., Yohannes, B., Hill, K. M., & Dietrich, W. E. (2016).  
590 Effects of coarse grain size distribution and fine particle content on pore fluid  
591 pressure and shear behavior in experimental debris flows. *Journal of Geophysical*  
592 *Research: Earth Surface*, *121*(2), 415–441. doi: 10.1002/2015jf003725
- 593 Kessler, M., Heller, V., & Turnbull, B. (2020). Grain Reynolds Number scale effects  
594 in dry granular slides. *Journal of Geophysical Research: Earth Surface*, *125*(1).  
595 doi: 10.1029/2019jf005347

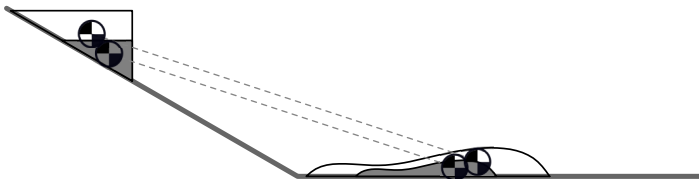
- 596 Legros, F. (2002). The mobility of long-runout landslides. *Engineering Geology*,  
597 *63*(3-4), 301–331. doi: 10.1016/s0013-7952(01)00090-4
- 598 Leonardi, A., Cabrera, M., Wittel, F. K., Kaitna, R., Mendoza, M., Wu, W., & Her-  
599 rmann, H. J. (2015). Granular-front formation in free-surface flow of concentrated  
600 suspensions. *Physical Review E*, *92*(5). doi: 10.1103/physreve.92.052204
- 601 Mangeney, A., Roche, O., Hungr, O., Mangold, N., Faccanoni, G., & Lucas, A.  
602 (2010). Erosion and mobility in granular collapse over sloping beds. *Journal of*  
603 *Geophysical Research*, *115*(F3). doi: 10.1029/2009jf001462
- 604 McDougall, S. (2017). 2014 canadian geotechnical colloquium: Landslide runout  
605 analysis — current practice and challenges. *Canadian Geotechnical Journal*,  
606 *54*(5), 605–620. doi: 10.1139/cgj-2016-0104
- 607 Perez, S., & Aharonov, E. (2015). Long runout landslides: a solution from granular  
608 mechanics. *Frontiers in Physics*, *3*. doi: 10.3389/fphy.2015.00080
- 609 Raymond, G. P. (2002). Reinforced ballast behaviour subjected to repeated load.  
610 *Geotextiles and Geomembranes*, *20*(1), 39–61. doi: 10.1016/s0266-1144(01)00024  
611 -3
- 612 Rickenmann, D. (2011). Runout prediction methods. In O. Hungr & M. Jakob  
613 (Eds.), *Debris-flow hazards and related phenomena* (pp. 305–324). Springer Berlin  
614 Heidelberg.
- 615 Staron, L., & Lajeunesse, E. (2009). Understanding how volume affects the mo-  
616 bility of dry debris flows. *Geophysical Research Letters*, *36*(12). doi: 10.1029/  
617 2009gl038229
- 618 Taylor-Noonan, A. M., Gollin, D., Bowman, E. T., & Take, W. A. (2021). The influ-  
619 ence of image analysis methodology on the calculation of granular temperature for  
620 granular flows. *Granular Matter*, *23*(4). doi: 10.1007/s10035-021-01153-y
- 621 Tayyebi, S. M., Pastor, M., & Stickle, M. M. (2021). Two-phase SPH numerical  
622 study of pore-water pressure effect on debris flows mobility: Yu Tung debris flow.  
623 *Computers and Geotechnics*, *132*, 103973. doi: 10.1016/j.compgeo.2020.103973
- 624 Turnbull, B., Bowman, E. T., & McElwaine, J. N. (2015). Debris flows: Experiments  
625 and modelling. *Comptes Rendus Physique*, *16*(1), 86–96. doi: 10.1016/j.crhy.2014  
626 .11.006
- 627 Voight, B., & Faust, C. (1982). Frictional heat and strength loss in some rapid land-  
628 slides. *Géotechnique*, *32*(1), 43–54. doi: 10.1680/geot.1982.32.1.43
- 629 Zhou, G. G. D., Li, S., Song, D., Choi, C. E., & Chen, X. (2018). Depositional  
630 mechanisms and morphology of debris flow: physical modelling. *Landslides*, *16*(2),  
631 315–332. doi: 10.1007/s10346-018-1095-9

Figure 1.

(a) definitions of landslide geometry statistics



(b) travel angle invariant with source volume



(c) travel angle variant with source volume

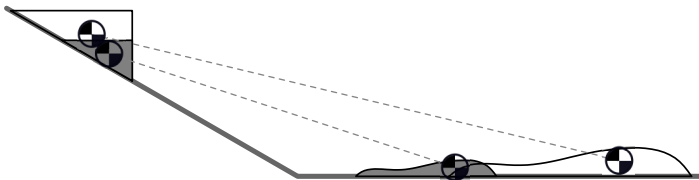


Figure 2.

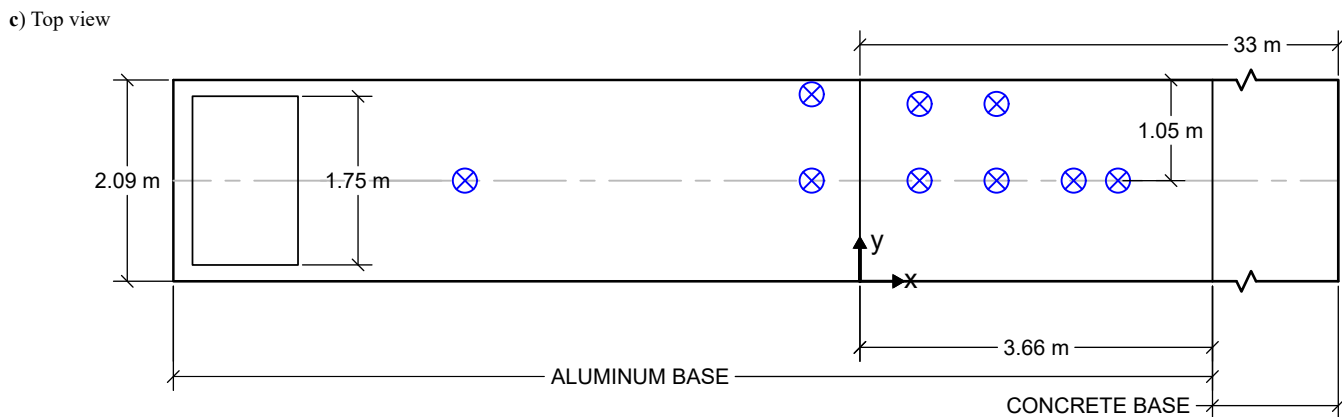
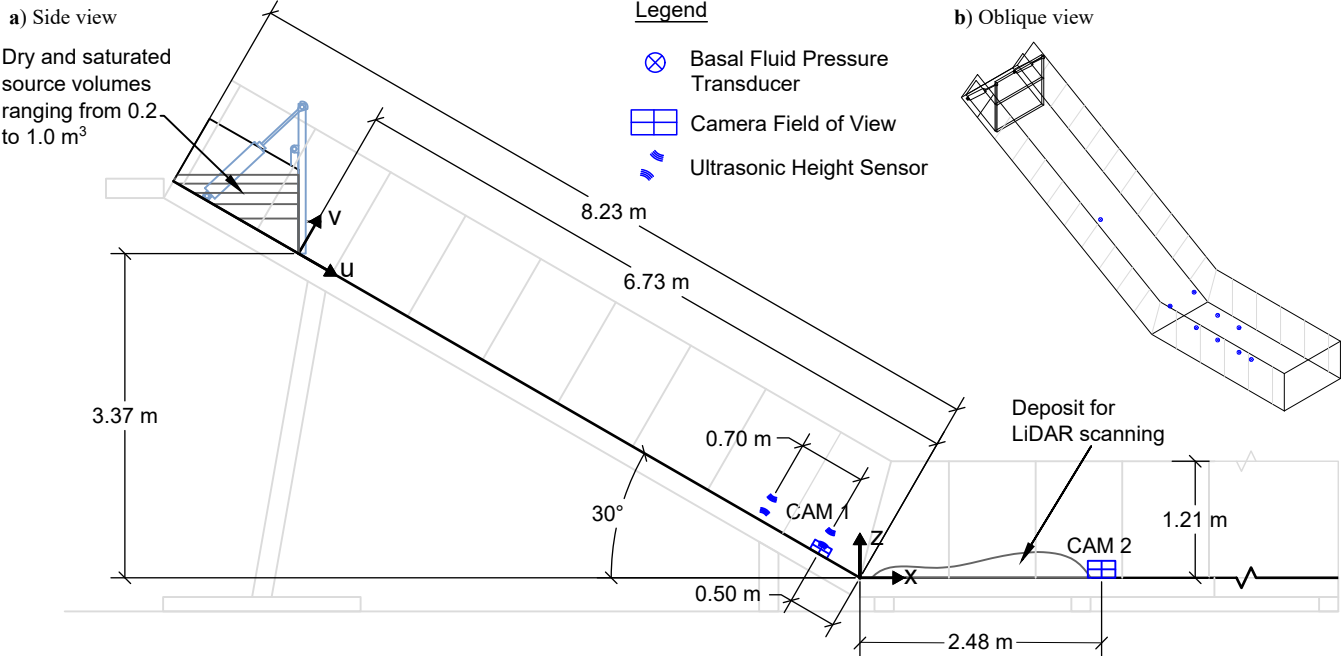


Figure 3.

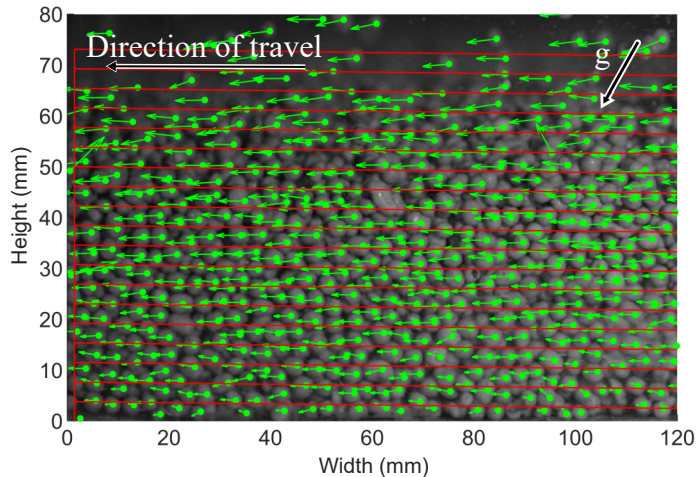
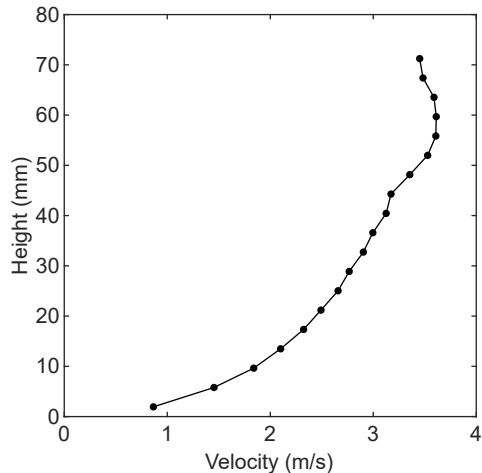
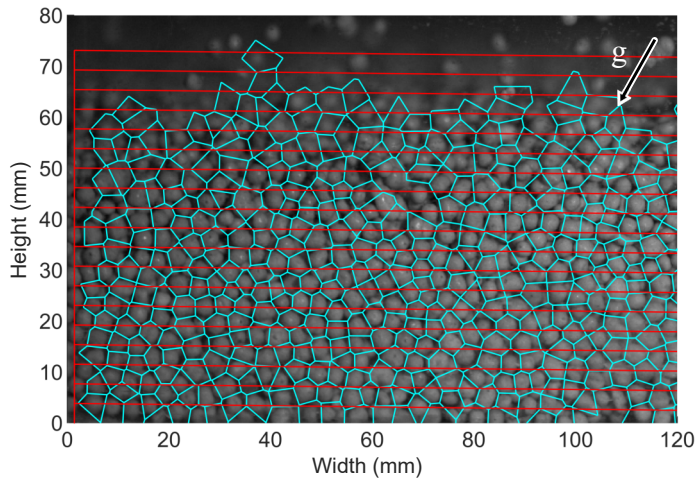
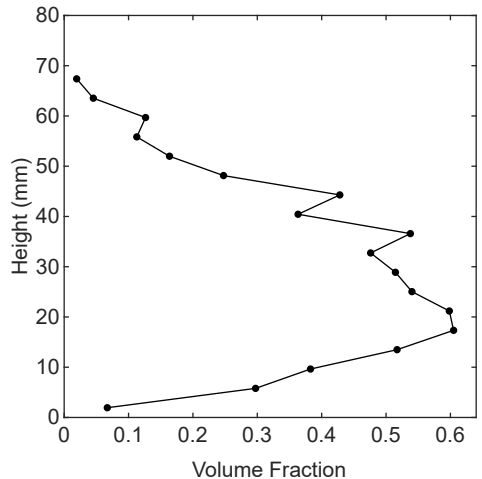
**(a)** Particle tracking vectors**(b)** velocity profile**(c)** High-speed video with Voronoi polygons drawn**(d)** volume fraction profile

Figure 4.

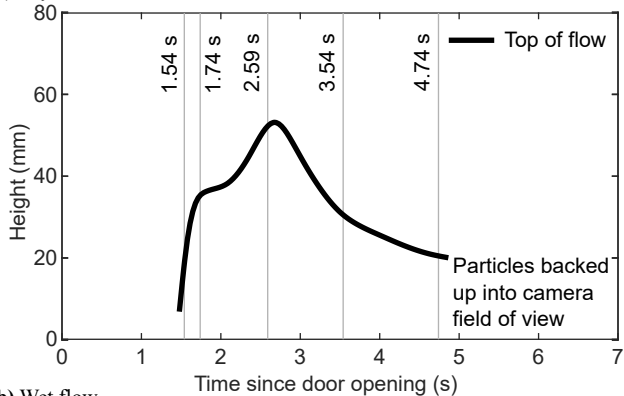
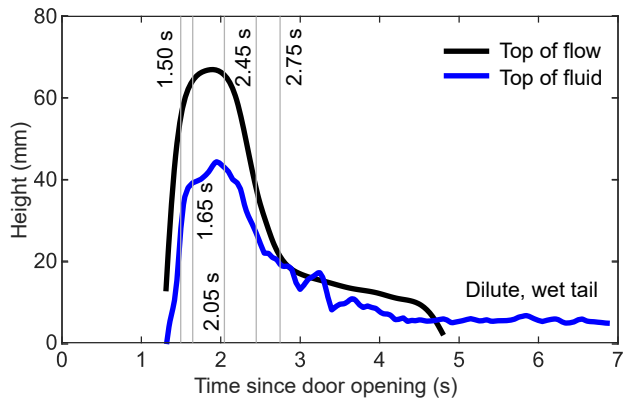
**a) Dry flow****b) Wet flow**

Figure 5.

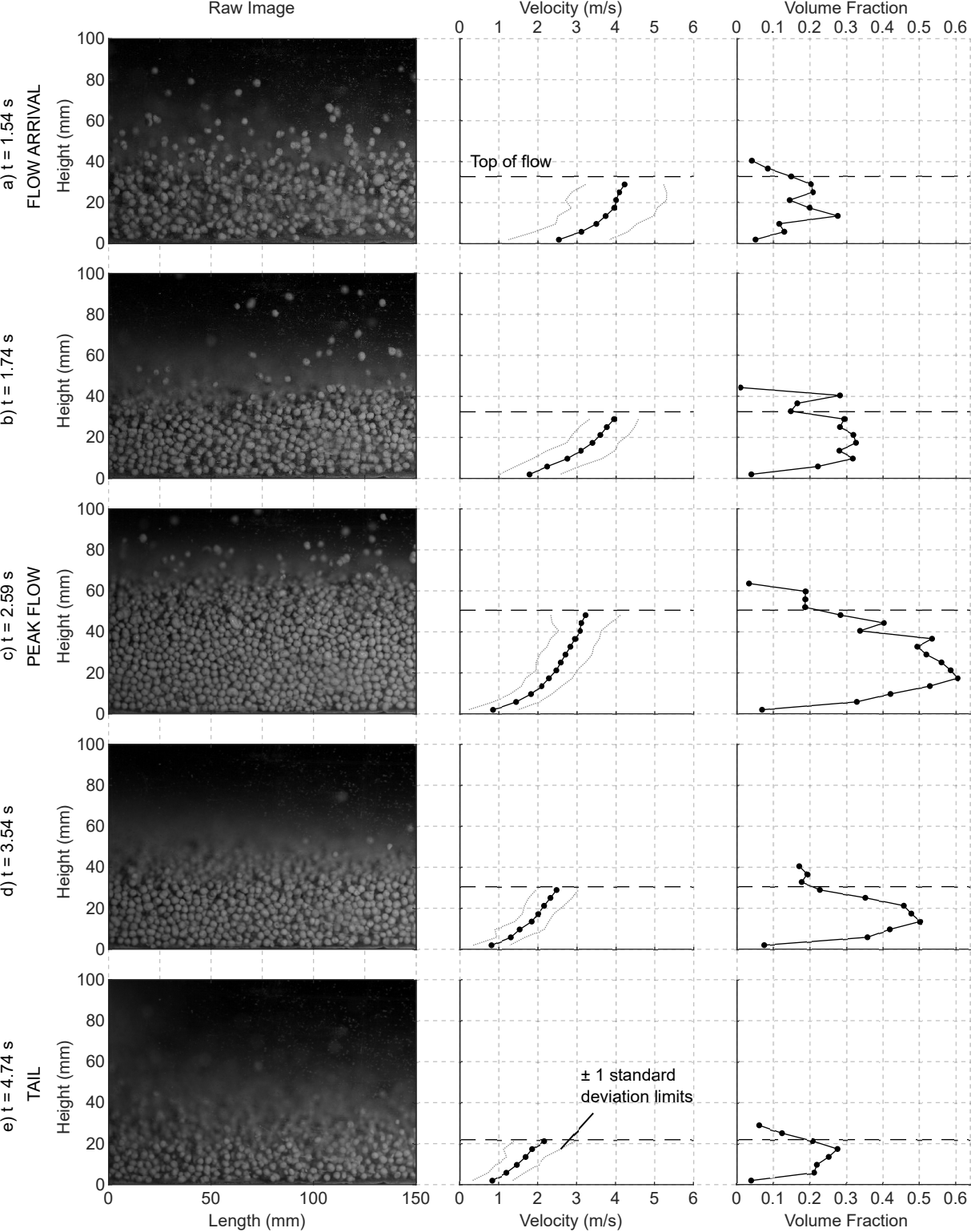


Figure 6.

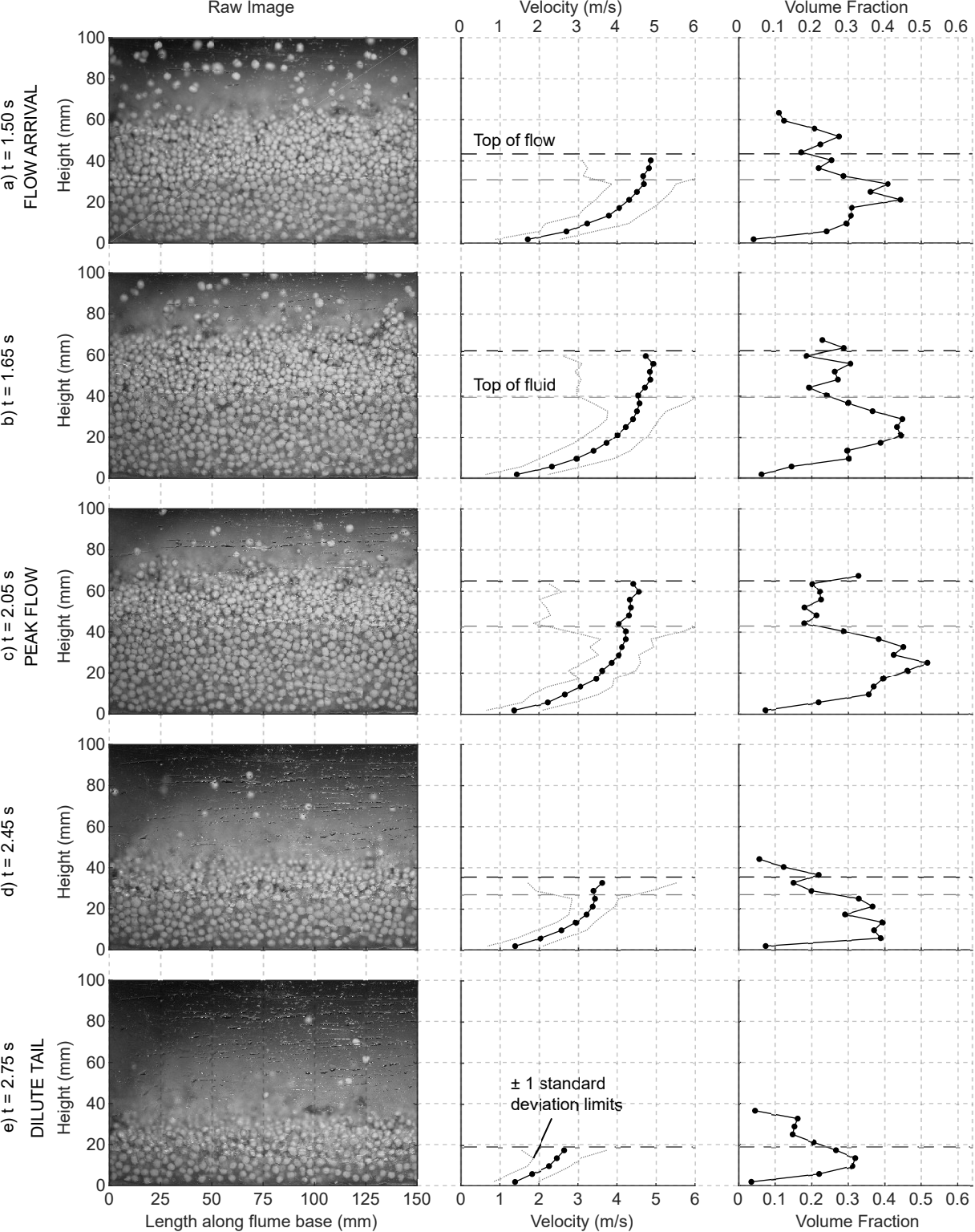


Figure 7.

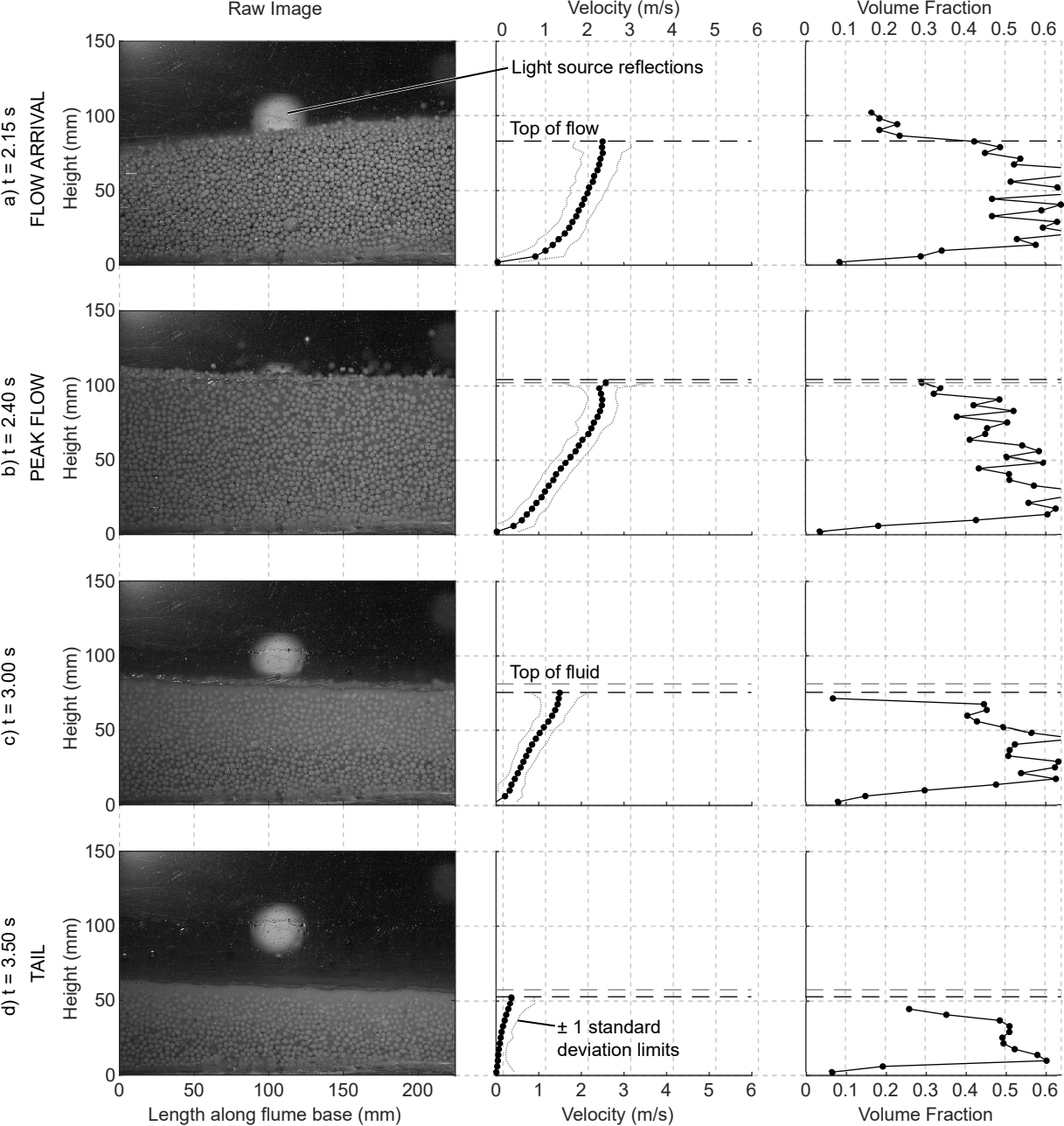


Figure 8.

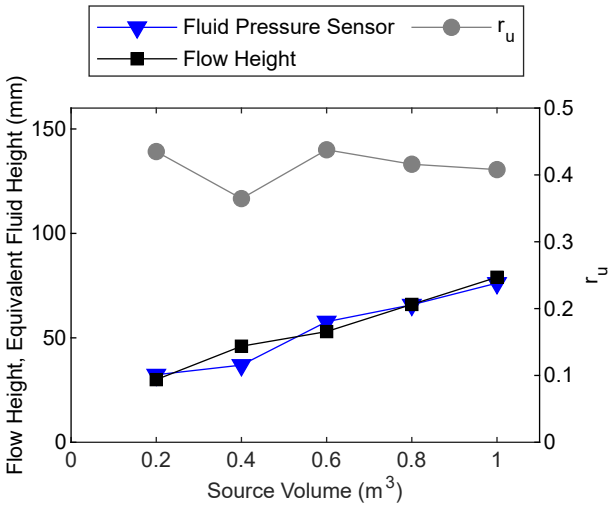
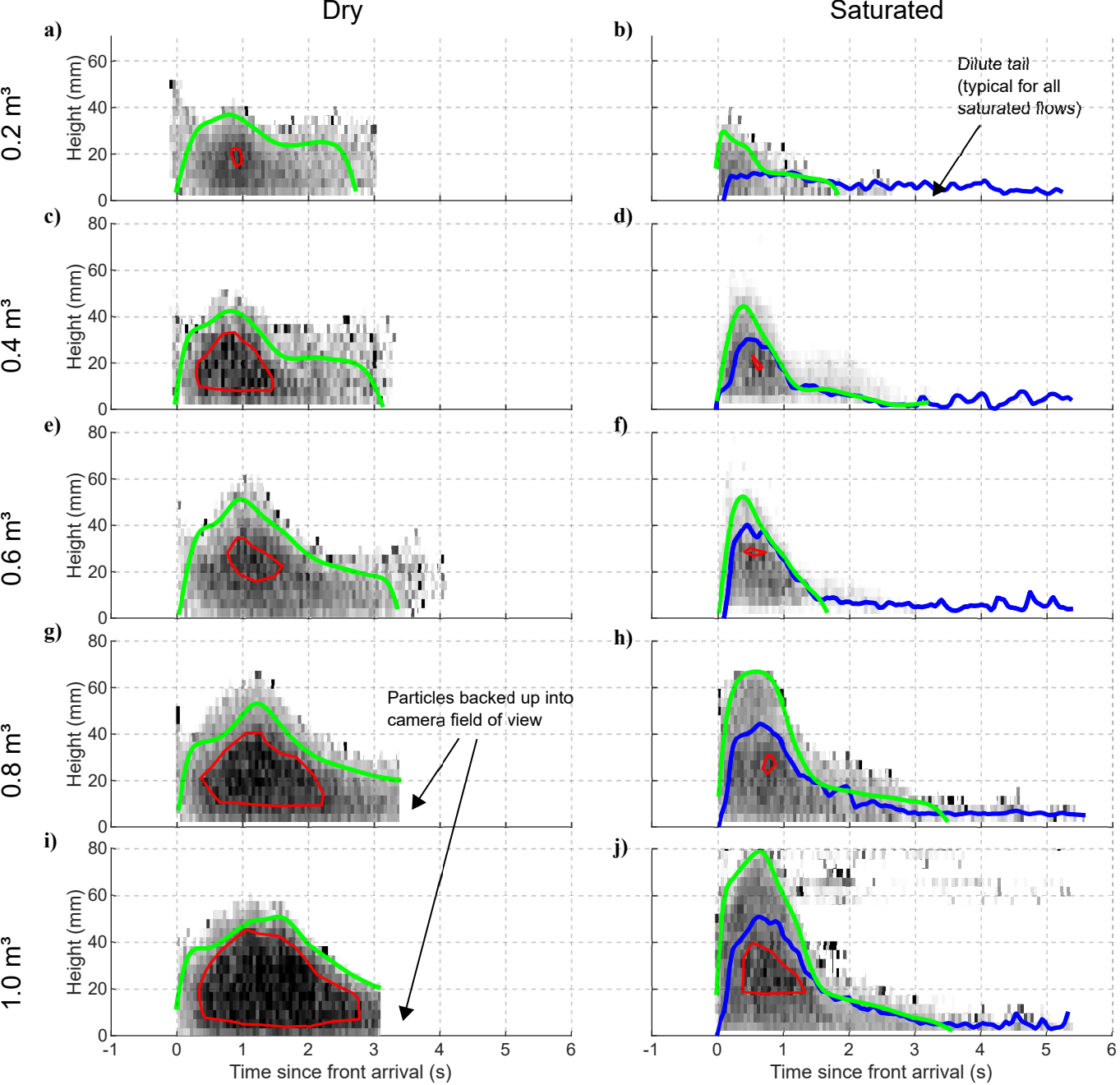


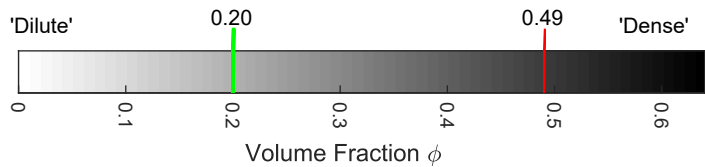
Figure 9.



Figure 10.



Colourmap scale represents Volume Fraction as determined by Voronoi-based method



Legend

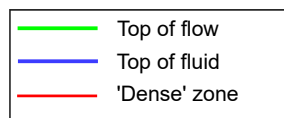
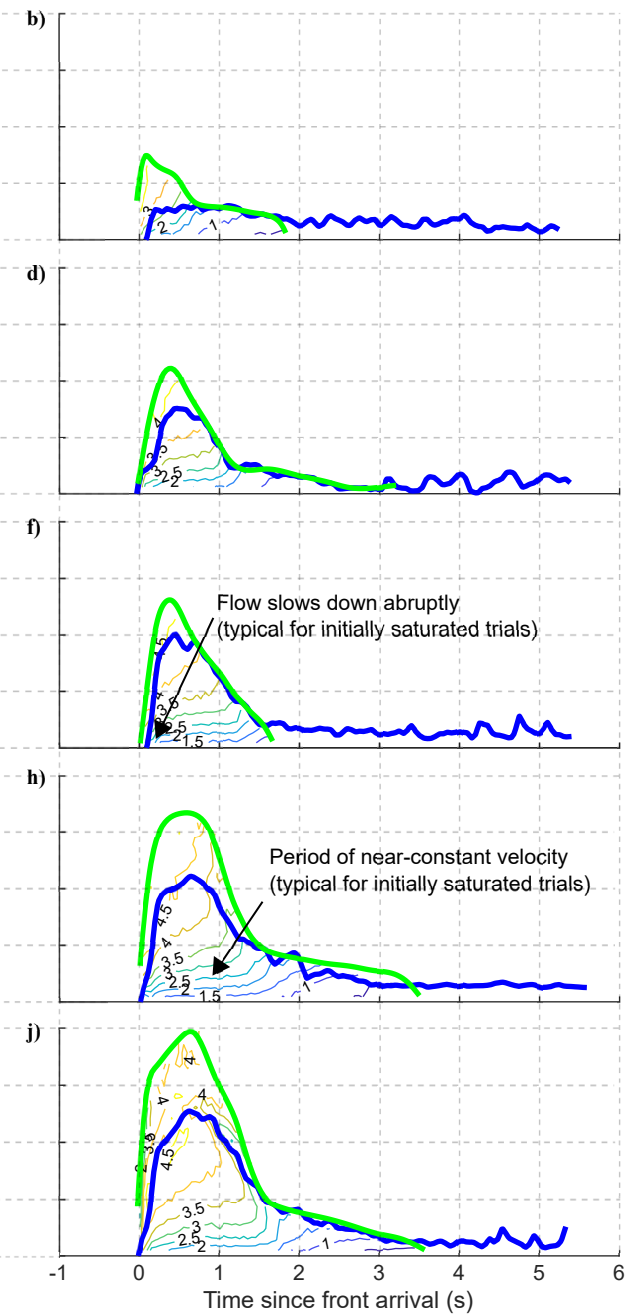
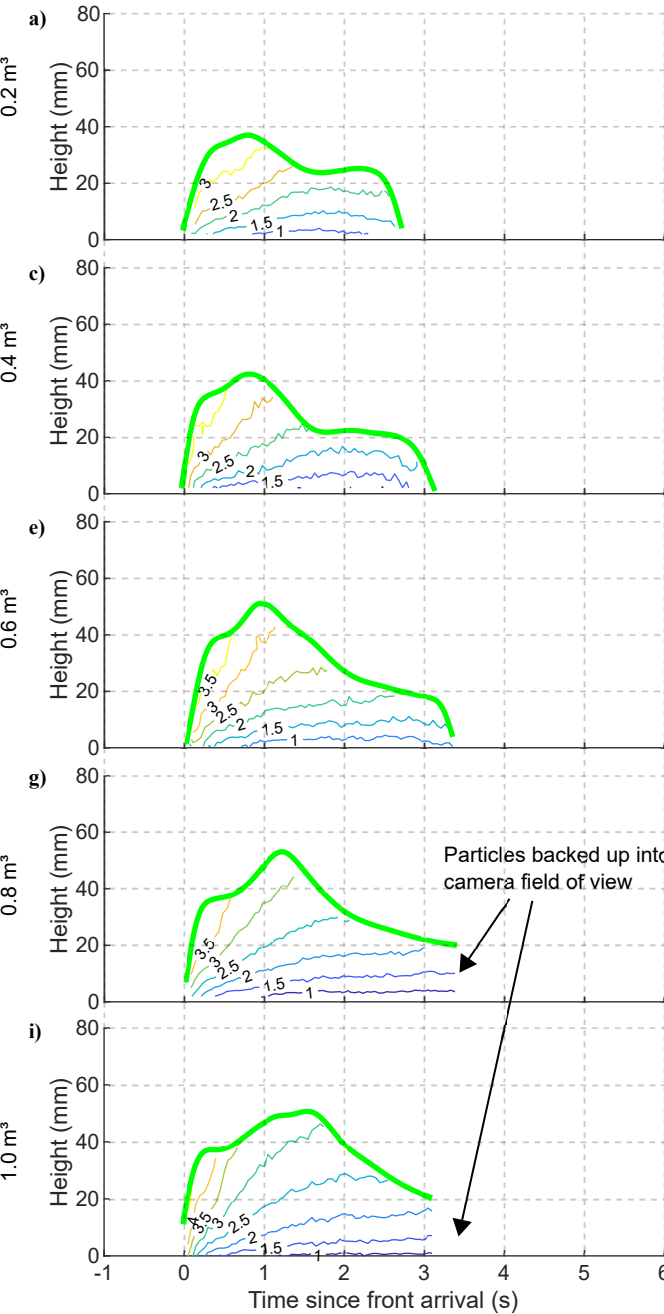


Figure 11.

Dry

Saturated



Contour lines represent streamwise flow velocity as determined by PTV method

Legend

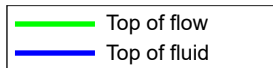
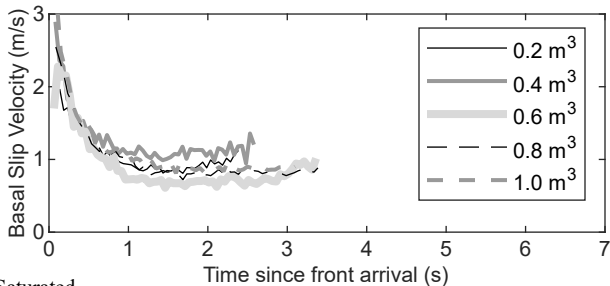


Figure 12.

a) Dry



b) Saturated

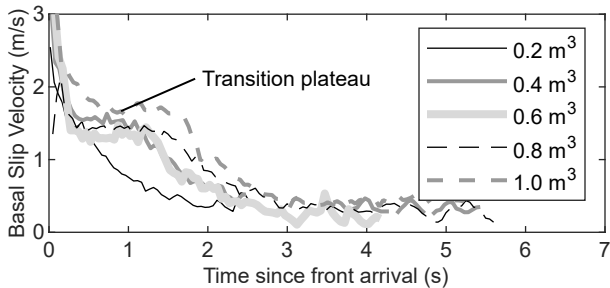
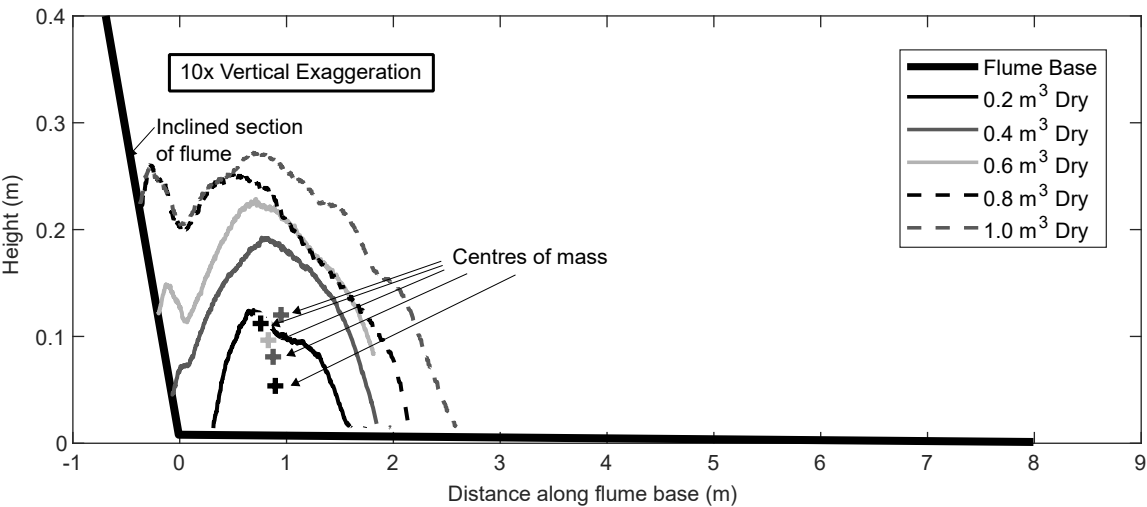


Figure 13.

(a) Dry trials



(b) Initially saturated trials

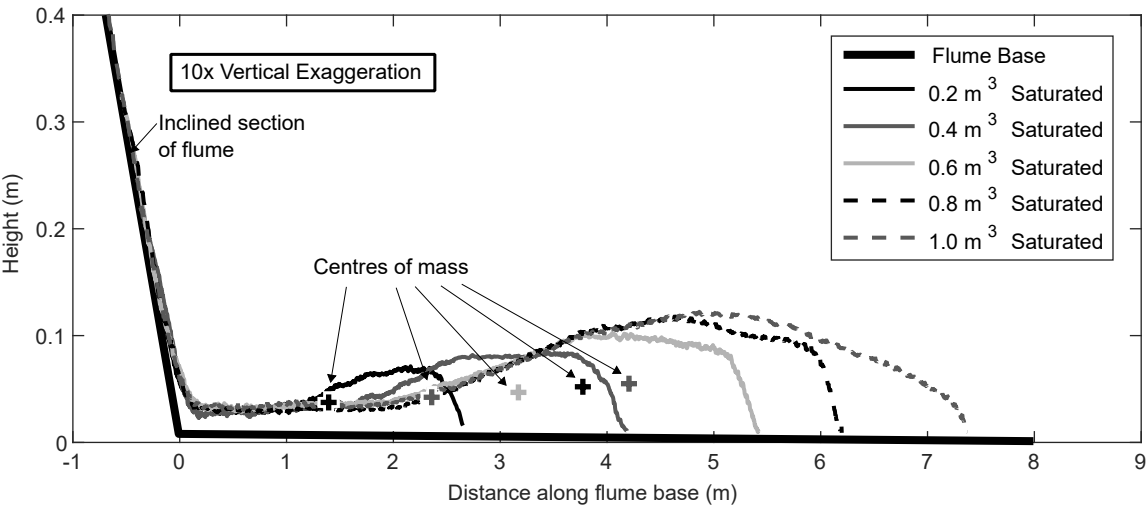


Figure 14.

